











Constraining the Number Density of the Accretion Disk Wind in Hercules X-1 Using Its Ionization Response to X-Ray Pulsations

P. Kosec^{1,2} , D. Rogantini³, E. Kara¹ , C. R. Canizares¹ , A. C. Fabian⁴ , C. Pinto⁵ , I. Psaradaki¹ , R. Staubert⁶ , and D. J. Walton⁷ 

¹ MIT Kavli Institute for Astrophysics and Space Research, Massachusetts Institute of Technology, Cambridge, MA 02139, USA; peter.kosec@cfa.harvard.edu

² Center for Astrophysics | Harvard & Smithsonian, Cambridge, MA 02138, USA

³ Department of Astronomy and Astrophysics, The University of Chicago, Chicago, IL 60637, USA

⁴ Institute of Astronomy, Madingley Road, Cambridge, CB3 0HA, UK

⁵ INAF—IASF Palermo, Via U. La Malfa 153, I-90146 Palermo, Italy

⁶ Institut für Astronomie und Astrophysik, Universität Tübingen, Sand 1, 72076 Tübingen, Germany

⁷ Centre for Astrophysics Research, University of Hertfordshire, College Lane, Hatfield, AL10 9AB, UK

Received 2024 January 2; revised 2024 June 21; accepted 2024 June 23; published 2024 August 22

Abstract

X-ray binaries are known to launch powerful accretion disk winds that can have a significant impact on the binary systems and their surroundings. To quantify the impact and determine the launching mechanisms of these outflows, we need to measure the wind plasma number density, an important ingredient in the theoretical disk wind models. While X-ray spectroscopy is a crucial tool for understanding the wind properties, such as their velocity and ionization, in nearly all cases, we lack the signal-to-noise ratio to constrain the plasma number density, weakening the constraints on the outflow location and mass outflow rate. We present a new approach to determining this number density in the X-ray binary Hercules X-1, by measuring the speed of the wind ionization response to the time-variable illuminating continuum. Hercules X-1 is powered by a highly magnetized neutron star, pulsating with a period of 1.24 s. We show that the wind number density in Hercules X-1 is sufficiently high to respond to these pulsations by modeling the ionization response with the time-dependent photoionization model TPHO. We then perform a pulse-resolved analysis of the best-quality XMM-Newton observation of Hercules X-1 and directly detect the wind response, confirming that the wind density is at least 10^{12} cm^{-3} . Finally, we simulate XRISM observations of Hercules X-1 and show that they will allow us to accurately measure the number density at different locations within the outflow. With XRISM, we will rule out ~ 3 orders of magnitude in density parameter space, constraining the wind mass outflow rate, energetics, and its launching mechanism.

Unified Astronomy Thesaurus concepts: [Accretion \(14\)](#); [Compact objects \(288\)](#); [Neutron stars \(1108\)](#)

1. Introduction

Accretion disk winds are wide-angle outflows launched from the disks of accreting compact objects. They may be driven by radiation pressure (Shakura & Sunyaev 1973; Proga et al. 2000), magnetic fields (Blandford & Payne 1982), thermally (Begelman et al. 1983), or by a combination of these different launching mechanisms. As the outflow lifts from the accretion disk, it is illuminated by the hot inner accretion flow and ionized. If it passes across our line of sight toward the ionizing source, the wind can imprint an absorption-line spectrum upon the continuum emission from the inner accretion flow, allowing us to detect the presence of the wind and to infer its physical properties. Such absorption spectra can readily be detected via X-rays, an energy band that contains line transitions spanning a very broad range of ionizations and plasma temperatures.

Ionized outflows have been detected to date in most types of accreting systems, including active galactic nuclei (AGNs; Weymann et al. 1991; Tombesi et al. 2010), tidal disruption events (Miller et al. 2015; Kosec et al. 2023c), X-ray binaries (Neilsen & Degenaar 2023), ultraluminous X-ray sources (ULXs; Pinto et al. 2016; Pinto & Kosec 2023), and even in

accreting white dwarfs (Greenstein & Oke 1982; Prinja et al. 2000).

In X-ray binaries, the first hints of disk wind absorption lines were detected in the late 1990s in the X-ray spectra provided by the CCD detectors on board ASCA (Ueda et al. 1998; Kotani et al. 2000). These lines were later better resolved by the high-resolution grating instruments on board the Chandra and XMM-Newton X-ray telescopes, allowing us to learn more about the outflow properties (e.g., Ueda et al. 2004). Nevertheless, even today, much is still unknown about these phenomena, including their launching mechanisms. More recently, powerful outflows have also been detected in X-ray binaries through UV, optical, as well as IR observations (Muñoz-Darias et al. 2019; Sánchez-Sierras & Muñoz-Darias 2020; Castro Segura et al. 2022). These newly detected outflows and the X-ray winds may be part of the same phenomenon, but showing up at different times, due to variations in the ionization field (Muñoz-Darias & Ponti 2022).

The winds seen in X-ray binaries have the potential to carry away a large fraction of the matter originally transferred into the accretion disk by the secondary star (e.g., Lee et al. 2002; Kosec et al. 2020). Therefore, they can significantly modify X-ray binary accretion flows (Tetarenko et al. 2018; Avakyan et al. 2024) and the binary evolution of these systems (Verbunt 1993; Ziółkowski & Zdziarski 2018; Gallegos-Garcia et al. 2023).



Original content from this work may be used under the terms of the [Creative Commons Attribution 4.0 licence](#). Any further distribution of this work must maintain attribution to the author(s) and the title of the work, journal citation and DOI.

High-resolution X-ray spectroscopy allows us to determine the outflow column density, ionization state, and projected velocity of the wind crossing our line of sight toward the X-ray source. Unfortunately, in a great majority of observations, it does not allow us to measure the wind number density. This is possible only in extraordinary quality X-ray spectra through density-sensitive spectral lines (Miller et al. 2006; Tomaru et al. 2023). However, even in these exceptional cases, photoexcitation by UV photons (Mewe & Schrijver 1978) must be considered, as it can complicate or invalidate the density measurement (e.g., Jimenez-Garate et al. 2005; Tomaru et al. 2023).

As a result, it is challenging to determine the distance of the outflow from the compact object and, consequently, to accurately determine its mass flow rate and energetics. This issue is also challenging the study of the wind-launching mechanisms. The wind-launching mechanisms predict different launching regions for the outflow (at different distances from the compact object), and thus determining the wind location can hold important clues as to its origin.

A promising way of determining the number density is by measuring how the wind responds to changes in the ionizing continuum. The plasma will attempt to adjust its ionization state to a variation in the illuminating radiation in order to return to photoionization equilibrium. The speed of this ionization adjustment directly depends on the plasma number density (Krolik & Kriss 1995). Therefore, the wind density can be measured by tracking the variation of the plasma ionization as a response to the time-variable X-ray flux using a time-dependent photoionization model (Nicastrò et al. 1999; García et al. 2013). In the last few years, a number of new time-dependent photoionization models have been developed to achieve these measurements (Rogantini et al. 2022; Luminari et al. 2023; Sadaula et al. 2023). Some of these models have recently been applied to constrain the number densities of warm absorbers in AGNs (Gu et al. 2023; Li et al. 2023).

In X-ray binaries, the wind number density is likely much higher than that of warm absorbers in AGNs (where densities of 10^{4-7} cm^{-3} have been measured; Gu et al. 2023). Consequently, its response to any flux variations should be much faster (on the order of seconds or even shorter), making it challenging to accumulate X-ray spectra at high-enough data quality and high-enough time cadence to allow us to track the ionization state variations. In other words, an extremely bright X-ray source is required, or an X-ray telescope with an extremely large effective area is needed to track these variations in “real time.”

Here, we present a completely different and new approach to this issue. Hercules X-1 (hereafter, Her X-1) is an X-ray pulsar with a detected accretion disk wind (Kosec et al. 2020) and a pulsation period of about 1.24 s (Tananbaum et al. 1972). Therefore, the disk wind of Her X-1 is repeatedly illuminated by a periodically time-variable X-ray beam from the pulsar. Assuming its number density is high enough, the wind will adjust its ionization state in response to the time-variable X-ray illumination, during each individual pulsation cycle. Hence, by stacking a large number of pulse periods and performing a pulse-resolved analysis, we can extract the response of the disk wind to the X-ray pulsation, on the timescale of a single 1.24 s X-ray pulsation, without the need for an extremely-large-effective-area telescope.

We further note that since the wind is observed in absorption—along our line of sight toward the X-ray source—the absorbing plasma sees nearly the same input (time-variable) X-ray continuum that we observe, only we observe it modified by the absorber itself. X-rays from other lines of sight (e.g., from large-scale X-ray emission) could contribute to our observed X-ray emission without ionizing the wind, but their amount is not likely to be significant compared with the primary X-ray emission in the case of Her X-1. Most of this primary emission is compact, originating from much closer to the neutron star than where the wind is located.

1.1. Her X-1

Her X-1, located at a distance of 6.1 kpc (Leahy & Abdallah 2014), is one of the first known X-ray pulsars, discovered in the early 1970s with the Uhuru satellite (Giacconi et al. 1972). It is most well known for its 35 days cycle of alternating high- and low-flux states (Katz 1973), which can be explained by the system being oriented almost edge-on and exhibiting a warped, precessing accretion disk (Gerend & Boynton 1976; Scott et al. 2000). The precession introduces periods of time during which the outer disk blocks our line of sight toward the inner accretion flow, thus resulting in a low state, and periods of time during which the neutron star is directly observable, resulting in a high state. Additionally, the warped disk precession results in a time-variable line of sight through the disk wind of Her X-1, uniquely allowing us to directly study its vertical structure and geometry (Kosec et al. 2023a).

The pulsations from Her X-1 have a period of 1.24 s and originate from the accretion column of the neutron star (Davidson & Ostriker 1973; Ghosh & Lamb 1979). The inner accretion disk is disrupted by the magnetosphere of the highly magnetized neutron star (10^{12} G; Truemper et al. 1978), and the infalling matter follows the magnetic field lines, creating the so-called accretion columns above the magnetic poles of the star. The accretion column has a nonspherical radiation beam pattern (Basko & Sunyaev 1975), and by rotating alongside the neutron star, it introduces regular X-ray pulsations at the neutron star rotation period, since the magnetic axis is misaligned with the rotation axis.

To judge the potential response of the wind to the X-ray pulsation of Her X-1, we first determine the most likely range of the wind number density. These limits are estimated from previous time-averaged X-ray observations in Section 2. Second, in Section 3, we use the recently developed time-dependent ionization model TPHO (Rogantini et al. 2022) to model the expected response of the wind, given the obtained density limits. We show that the wind density is high enough to quickly respond to the X-ray pulsations with a period of 1.24 s, at least in some of the archival X-ray observations. We then perform a pulse-resolved analysis of the highest-quality X-ray observation of the Her X-1 wind and directly detect this effect. In Section 4, we describe our data reduction and preparation methods, and in Section 5 we list our spectral modeling methods and the analysis results.

In 2023, the XRISM satellite (XRISM Science Team 2020) launched and began operations. Thanks to its exceptional spectral resolution in the hard-X-ray band (2–10 keV), XRISM will have excellent capabilities to study the wind response to the Her X-1 pulsations. In Section 6, we perform XRISM observation simulations, showing that the instrument will easily

detect this effect. Finally, in Section 7, we discuss these results, and in Section 8, we give the conclusions of our study.

2. Prior Constraints on Wind Density

In order to model the response of the disk wind in Her X-1 to its X-ray pulsations (in the following section), we put limits on the wind number density. We derive these limits from other physical wind parameters, which were measured by Kosec et al. (2023a). In that paper, we showed that the wind properties evolve systematically with the precession phase, as our line of sight moves due to the warped disk precession and samples the wind at different heights above the disk. In Appendix A, we estimate representative wind properties at different precession phases, corresponding to representative wind properties at different heights above the warped disk. We estimate the representative wind column density, ionization parameter, and isotropic mass outflow rate. Then we use these “average” parameters to infer lower and upper limits on the wind number density at a range of precession phases, using the following arguments.

The constraint with the highest confidence level (but not the most restrictive) on the lower limit of the wind number density comes from the photoionization balance. The spectral modeling allows us to determine the wind column density and its ionization parameter, defined as

$$\xi = \frac{L_{\text{ion}}}{nR^2}, \quad (1)$$

where L_{ion} is the ionizing luminosity (measured between 13.6 eV and 13.6 keV), n is the plasma density, and R is the distance of the absorber from the ionizing source. Using the definition of the column density $N_{\text{H}} = n\Delta R$, where ΔR is the thickness of the absorber, we can calculate the number density, such as

$$n = \frac{\xi N_{\text{H}}^2}{L_{\text{ion}}} \left(\frac{\Delta R}{R} \right)^{-2}. \quad (2)$$

Here, the $\Delta R/R$ is the relative thickness of the absorbing layer, which naturally cannot be larger than 1. By taking this limiting value, we can calculate the minimum absorber number density:

$$n_{\text{min}} = \frac{\xi N_{\text{H}}^2}{L_{\text{ion}}}. \quad (3)$$

This lower limit on density is shown in Figure 1 in the red color for a range of disk precession phases.

A stricter lower limit on the wind number density is obtained by considering the maximum mass outflow rate. First, the outflow rate cannot exceed the mass transfer rate through the outer accretion disk (assuming a long-term stable accretion flow). Second, the mass outflow rate at greater heights above the disk (further along the streamlines) should not exceed the outflow rate at lower heights. Following the derivation of Kosec et al. (2020), the mass outflow rate can be calculated from the measured wind quantities as

$$\dot{M}_{\text{out}} = 4\pi\mu m_{\text{p}}v \frac{L_{\text{ion}}}{\xi} C_{\text{V}} \frac{\Omega}{4\pi} = \dot{M}_{\text{iso}} C_{\text{V}} \frac{\Omega}{4\pi}, \quad (4)$$

where v is the wind velocity, C_{V} is the volume-filling factor, Ω is the solid angle into which the outflow is being launched, μ defines the mean atomic mass (~ 1.2 , assuming solar abundances), and m_{p} is the proton mass. \dot{M}_{iso} is the isotropic

mass outflow rate, assuming a maximum volume-filling factor (100%) and a 4π launching solid angle. Kosec et al. (2023a) found that the volume-filling factor C_{V} must decrease with precession phase. Otherwise, the mass outflow rates at greater heights above the disk would by far exceed the mass transfer rates through the disk itself, as well as the outflow rates at lower heights.

Therefore, by assuming that the solid angle of the outflow does not change with height above the disk, and given the fact that the mass outflow rate should not increase upward in the flow, we can calculate the ratio of volume-filling factors C_{V} for points at various heights above the disk. We use the calculated \dot{M}_{iso} rates (Appendix A) to get the ratios of C_{V} , which should be proportional to the relative thickness of the outflow $\Delta R/R$ (since $\Omega \sim \text{constant}$). As a result, we can determine the relative thickness ratio for the wind measurement points in comparison with the point at the precession phase 0.03 (see Figure 1), which can be substituted in Equation (2). This allows us to tighten the photoionization balance limits on the wind density, by taking the most relaxed case scenario of $\Delta R/R = 1$ at a precession phase of 0.03. These tightened density lower limits are shown in Figure 1 in the blue color. However, we note that this is not a hard lower limit on the wind density (in contrast to the photoionization balance limit). It is possible to avoid this limit if the wind solid angle Ω varies with height above the disk.

Finally, a soft upper limit on the number density can be derived from the outflow velocity and by assuming that this is not a failed outflow. The projected line-of-sight velocity of the Her X-1 wind is mostly between 200 and 800 km s⁻¹. Following the calculations of Kosec et al. (2023a), even assuming the maximum relative thickness ($\Delta R/R = 1$), which results in the maximum possible outflow distance from the neutron star, the escape velocity near the base of the wind (at low heights above the disk) is about 2000 km s⁻¹. The outflow can still be successfully launched, as we are only observing the line-of-sight velocity component and do not measure any vertical (due to the high inclination of Her X-1) and especially toroidal (Keplerian) components. However, it is unlikely that the outflow of such a low projected velocity could be launched at much lower radii in the disk, where the required escape velocity is much higher—the velocity projection angle would have to be extreme.

For this reason, we can put a soft lower limit on the outflow location (which in turn corresponds to a soft upper limit on the number density) by considering the outflow at the point where it is observed closest to the neutron star (at the lowest precession phase, 0.03, in Figure 1). Here, we assume that the outflow can only be launched from a location where the escape velocity is less than 4000 km s⁻¹, double the velocity that we obtain by taking the maximum outflow distance at these low precession phases. If the outflow is located even closer to the neutron star than this assumption, it is not a failed wind (i.e., its velocity is above 4000 km s⁻¹), and it shows a typical line-of-sight velocity of 500 km s⁻¹, the wind streamline direction must make an angle of at least 83° with respect to our line of sight.

From this assumption of the maximum escape velocity, we can calculate the ratio of the maximum and the minimum outflow distance, which is 4. This is also the inverse of the minimum outflow relative thickness: $\Delta R/R = 0.25$. Finally, using Equation (2), we can calculate the wind density at this

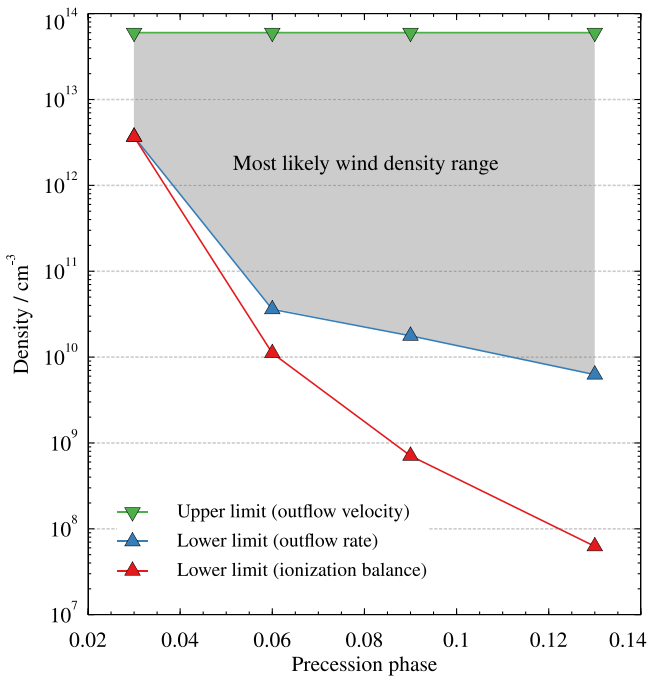


Figure 1. The upper and lower limits on the wind number density at different Her X-1 precession phases. The limits are determined by various considerations in Section 2, using the representative outflow properties measured in previous studies of Her X-1. The shaded region represents the most likely wind number density range.

minimum distance point, which corresponds to the maximum possible wind density of about $6 \times 10^{13} \text{ cm}^{-3}$ at the precession phase of 0.03. At greater precession phases than 0.03, corresponding to greater heights above the disk, it is unlikely that the plasma density would increase compared with the density at the lower heights. Therefore, $6 \times 10^{13} \text{ cm}^{-3}$ is the upper limit on the wind density throughout all precession phases. It is shown in green in Figure 1. We stress that this is a very soft upper limit on the outflow number density. Its value could in practice be higher. However, in that case, the wind would most likely be a failed outflow and not escape the system at all. This was suggested by Nixon & Pringle (2020).

We conclude that the most likely wind density is between 10^9 and 10^{14} cm^{-3} across all heights above the disk. The density must be rather high (about 10^{13} cm^{-3}) near the base of the wind, but it may decrease significantly as the outflow climbs to greater heights above the disk. Such high number densities will result in much faster ionization responses (on timescales of seconds, similar to the Her X-1 pulse period, or even lower) compared with warm absorbers in AGNs, where densities of 10^{4-7} cm^{-3} result in the response times of 10^{3-5} s or longer (Gu et al. 2023; Li et al. 2023).

3. Time-dependent Photoionization Modeling

In the previous section, we estimated the most likely wind number density range at different phases of the disk precession cycle. Now we can simulate how the wind will respond to X-ray flux variations at the 1.24 s pulsation period. We use the recently developed time-dependent photoionization model TPHO (Rogantini et al. 2022), which is publicly available in the SPEX package (Kaastra et al. 1996). TPHO simulates the response of a slab of plasma, which is originally assumed to be in photoionization balance, to a time-variable light curve. If

provided with a constant light curve, TPHO will reproduce an equivalent transmission spectrum to the one calculated by the equilibrium photoionization spectral model PION (Mehdipour et al. 2016) in SPEX.

We simulate the response of the disk wind to X-ray pulsation at the Her X-1 precession phase of about 0.03, when the wind column density is roughly 10^{23} cm^{-2} and its ionization parameter is $\log(\xi/\text{erg cm s}^{-1}) = 3.77$ (Appendix A). This precession phase is chosen because the wind column density is at its highest, and so the wind absorption lines are the strongest (and most easily detectable).

Another input to TPHO is the illuminating X-ray continuum. We take the best-fitting continuum spectral model of observation 0865440101 (the highest-quality XMM-Newton observation of the Her X-1 disk wind), which we analyzed in Kosec et al. (2023a) and which occurred exactly at the precession phase of 0.03.

The X-ray pulsation light curve is obtained by performing a pulse-resolved analysis of the European Photon Imaging Camera (EPIC) pn⁸ data from this observation, described in the following two sections of this paper. We take the unabsorbed 0.5–10 keV luminosity of Her X-1 after accounting for disk wind and Galactic absorption (see Section 5 for further details) as the input light curve for TPHO. We do not use the X-ray count rate, as this quantity is affected by the energy-dependent effective area of XMM-Newton, considering the variations in the spectral shape of the Her X-1 continuum over the pulsation period. We also do not use the extrapolated total (0.1–100 keV) Her X-1 luminosity, because this is not as accurately measured by EPIC pn as the narrower 0.5–10 keV range (which is fully covered by EPIC pn). Using the 0.5–10 keV band is a conservative estimate of the level of flux variations in Her X-1, considering that its pulsed fraction increases with energy (Ferrigno et al. 2023). Including harder energies would thus increase the flux variation (the total pulsed fraction). Larger flux variations lead to greater changes in wind ionization, and so our approach leads to a conservative estimate of how strongly the wind ionization can vary over the Her X-1 pulse period.

The final input of TPHO is the plasma number density, which determines how quickly the outflow can react to any variation of ionizing luminosity. We test the wind response for a range of wind densities based on the findings of the previous section: 10^9 , 10^{10} , 10^{11} , 10^{12} , 10^{13} , 10^{14} , and 10^{15} cm^{-3} . Such a broad range of values should encompass any possible Her X-1 wind density, even accounting for uncertainties in the approach adopted in the previous section.

One significant drawback of the current version of TPHO is that the model assumes a constant spectral energy distribution (SED) of the illuminating continuum throughout the time evolution of the plasma ionization state. This approximation is not fully valid for Her X-1, where the X-ray spectrum varies with pulse phase. Specifically, the soft X-rays pulsate out of phase in comparison with the hard X-rays (e.g., Zane et al. 2004). This spectral variation is shown in Appendix B. Nevertheless, TPHO will still provide an extremely useful view of the wind plasma response to the Her X-1 X-ray pulsation. However, given the SED limitation at this stage, we prefer not to directly fit the X-ray spectra with TPHO to determine the best-fitting wind density, as this measurement would not be

⁸ EPIC pn is the best instrument for this analysis, with sufficient temporal resolution to resolve the 1.24 s pulsation.

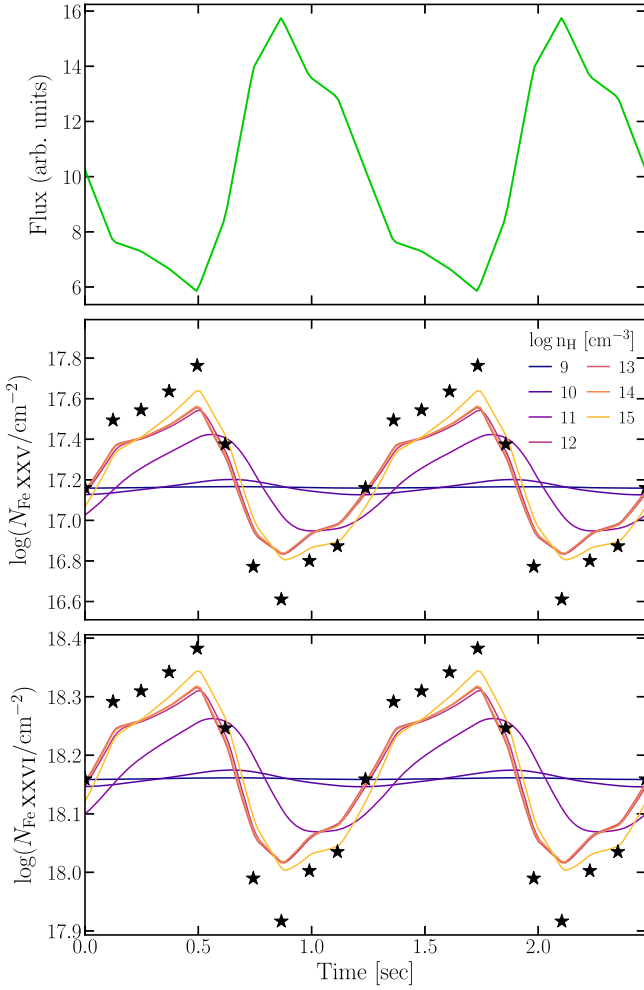


Figure 2. TPHO simulations of the ionized disk wind response to the Her X-1 X-ray pulsations. The top panel shows the intrinsic 0.5–10 keV pulsation light curve (two cycles are shown). The middle and the bottom panels show the column densities of Fe XXV and Fe XXVI ions, respectively. The black stars show the response of plasma in immediate photoionization equilibrium, while the lines of different colors show plasma of different number densities (from 10^9 to 10^{15} cm^{-3}).

reliable. A future version of TPHO (D. Rogantini et al. 2024, in preparation) will include a time-variable source SED.

We input the spectral continuum model, the disk wind properties, its number density, and the X-ray pulsation light curve to TPHO. Then the plasma is evolved for five X-ray pulsation cycles (about 6 s in real Her X-1 pulsation time) to obtain a stable wind response. Afterward, the wind properties are extracted from the following two X-ray pulsation cycles. We particularly follow the Fe XXV and Fe XXVI ion column densities, as the Fe XXV (6.67 keV) and Fe XXVI (6.96 keV) transitions are the strongest resolved disk wind absorption lines in the EPIC pn energy band. We note that the outputs from the TPHO simulations are the ionic concentrations of different ions relative to hydrogen. We convert these concentrations to ionic column densities using the best-fitting wind column density ($N_{\text{H}} = 10^{23}$ cm^{-2}) and the best-fitting Fe abundance from observation 0865440101. This Fe abundance (Fe/O = 2.1) was determined by a time-averaged wind abundance analysis by Kosec et al. (2023a). This simulation procedure is performed for all the wind number densities tested.

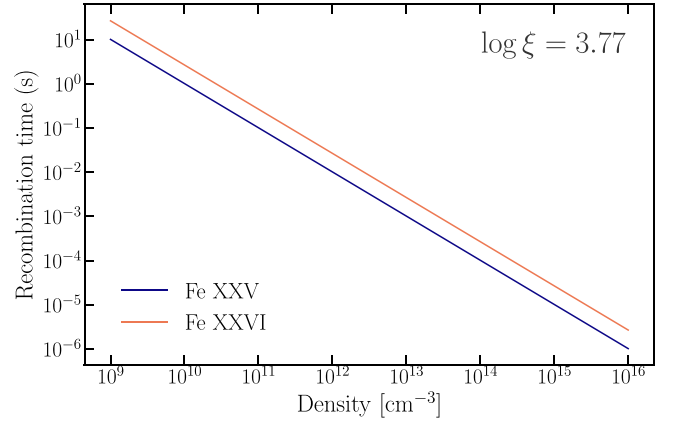


Figure 3. Fe XXV (blue) and XXVI (orange) ion recombination times vs. plasma number density n_e , which can be calculated as $t_{\text{rec}} = (\alpha_{\text{rec}} n_e)^{-1}$, where α_{rec} is the radiative recombination coefficient (e.g., Nicastrò et al. 1999).

We show the simulation results in Figure 2. The top panel shows the input light curve (of unabsorbed 0.5–10 keV luminosity) over the X-ray pulsation period (two cycles are shown). The middle and the bottom panels show the column density in the Fe XXV and Fe XXVI ions, respectively, over the pulse period. The colors show the responses of plasma of different number densities, while the stars show the column densities for plasma in immediate photoionization equilibrium. For low plasma densities (10^{10} cm^{-3} and lower), the wind density is so low that it basically does not respond to the X-ray pulsation at all. For higher but still low densities (10^{11} cm^{-3}), the response is weak and significantly delayed in comparison with the pulsation light curve. For higher densities (10^{12} cm^{-3} and higher), the response becomes faster and stronger, more in line with the response of plasma in immediate photoionization balance.

The shapes of the Fe XXV and XXVI responses can be explained by analyzing how their ionic concentrations respond to a change in the plasma ionization parameter. This is explored in Appendix C. From Figure 12, we can see that in this high-ionization regime at $\log(\xi/\text{erg cm s}^{-1})$ of around 3.8, most Fe atoms are fully ionized (in the Fe XXVII state). Assuming the number density is sufficient, an increase in the incident flux leads to a rise in the ionization parameter. This results in a decrease in the ionic concentrations of both Fe XXV and XXVI, reducing their column densities. A return into the original (lower) incident flux decreases the ionization parameter. As a result, some of the Fe XXVII atoms recombine into the Fe XXV and XXVI states, increasing the column densities in these transitions.

An alternative way to show the speed of the disk wind response to any variations in ionizing flux is through the recombination times in different transitions. This is shown in Figure 3 for the Fe XXV and Fe XXVI transitions, assuming wind properties similar to those at the precession phase of 0.03. For low wind densities ($n < 10^{10}$ cm^{-3}), the wind response is longer than 1 s, as long or longer than the 1.24 s pulsation period. For high number densities (10^{12-13} cm^{-3} and higher), both the Fe XXV and XXVI recombination times are very fast, lower than 0.01 s, and it will be challenging to measure them directly.

Given the wind density limits we obtained in the previous section, we can make the following predictions about the wind response to the X-ray pulsation of Her X-1. At low precession

phases, the density is expected to be high (above 10^{12} cm^{-3}), and so the wind should respond to the pulsation and it should respond almost immediately. The strength of the response is related to the ratio of the minimum and the maximum illuminating flux during the pulsation cycle. For plasma in immediate photoionization equilibrium, a ratio of $F_{\text{max}}/F_{\text{min}} \sim 2\text{--}3$ (appropriate for Her X-1) should correspond to a change in the ionization parameter $\Delta \log(\xi / \text{erg cm s}^{-1}) \sim 0.3\text{--}0.5$. This effect should therefore be directly observable, even with current X-ray telescopes, as will be shown in the following sections.

At higher precession phases, the wind absorption is weaker (Kosec et al. 2023a), complicating the possibility of detection of any pulse-resolved variability. However, the wind density may also be lower, as low as 10^9 cm^{-3} for precession phases around 0.13. If the wind density indeed decreases with height above the disk, as is likely, its density may cross from the range when the response is immediate, through a range when the response is significantly delayed and washed out, to a range when it stops responding altogether to the X-ray variations.

4. Data Reduction and Preparation

The wind absorption lines and their strengths evolve with the Her X-1 precession phase. As the measurement of the variation in the wind ionization state over the pulsar rotation period is quite challenging using the current X-ray instruments, we analyze only the observation with the highest signal-to-noise ratio (S/N) in the wind absorption lines. This is XMM-Newton (Jansen et al. 2001) observation 0865440101, which occurred very close after the Her X-1 turn-on into the main high state and covers low precession phases around 0.02–0.04. The observation began on 2020 August 10 (MJD = 59071) and lasted for 126 ks. The Reflection Grating Spectrometer (RGS; den Herder et al. 2001) light curve of this observation is shown in the left part of Figure 2 in Kosec et al. (2022). For this analysis, we only extract the high-flux period with a duration of about 50 ks in the second half of the observation, not including a dipping period at the end of the observation. We do not analyze the low-flux periods, as their S/N is much lower. Additionally, the dipping periods contain highly variable, low-ionization, and neutral absorption originating at the outer edge of the Her X-1 disk, complicating the spectral analysis of the disk wind, and so are also ignored.

The observation files were downloaded from the XMM-Newton Science Archive and reduced using SAS V20, CALDB, as of 2023 February. We perform a pulse-resolved extraction, during which we split the X-ray period of Her X-1 into 10 pulse phase bins of equal length (about 0.124 s). The number of phase bins was chosen as a compromise between the bin time resolution and the S/N. In order to perform this split accurately, we first determined the precise Her X-1 pulsation period at the time of the observation. Initially, the photon arrival times were corrected into solar system barycenter, using the BARYCEN tool with the DE200 ephemeris. Then we corrected the photon arrival times for the orbital motion of Her X-1 using the orbital solution of Staubert et al. (2009). Finally, we used the EPOCH_FOLDING_SEARCH function within the Stingray package (Huppenkothen et al. 2019a, 2019b) to determine the precise period of Her X-1 during observation 0865440101. By locating the peak of the χ^2 epoch-folding statistics, we found $P = 1.23771944(2) \text{ s}$, which is in very good agreement with the measurements around MJD = 59071 (2020

Table 1
Details of Pulse-resolved Data Extraction

Pulse Phase Bin	Count Rate/s	Columns Excluded
0	402.9	0
1	390.5	0
2	438.7	0
3	438.5	0
4	389.7	0
5	468.7	0
6	388.8	2
7	400.3	2
8	481.6	0
9	451.5	0

Note. For each pulse phase bin, the net count rates are listed after any pileup correction, as well as the number of central columns excluded from the source region to mitigate pileup.

August 10) by the Fermi/Gamma-ray Burst Monitor Pulsar Project (Finger et al. 2009). Using this timing solution, we produced Good Time Interval files containing the split times for the 10 pulse phase bins throughout the full XMM-Newton observation.

We use data from the EPIC pn instrument (Strüder et al. 2001). We are unable to use any RGS data for the pulse-resolved analysis because the frame time of the RGS, which was operated in the standard spectroscopy mode, is too long (frame times of 4.8 s for RGS1 and 9.6 s for RGS 2). We also do not use EPIC metal oxide semiconductor (MOS) data, as they are too piled up. EPIC pn was used in the timing mode during the analyzed observation, to minimize the effect of pileup. The data were reduced using the EPPROC routine and only events of PATTERN ≤ 4 (single and double) were accepted as valid events. We produced a background light curve of the analyzed observation segment using the EVSELECT routine, but did not identify any periods of high background flaring.

Despite the usage of the timing mode, some of the EPIC pn spectra are piled up. The pulse-resolved analysis allows us to apply different source regions for different pulse phase bins, depending on their photon count rate (and the amount of pileup). For those phase bins not affected significantly by pileup, the source regions are rectangles centered on the core of the point-spread function (PSF). For the two phase bins significantly affected by pileup (bins 6 and 7, with uncorrected count rates of $700\text{--}800 \text{ s}^{-1}$), we removed the central two columns. In both cases, the background regions were rectangular regions composed of a few columns as far away from the core of the source PSF as possible. Since Her X-1 is an extremely bright source, the background flux was not comparable to the source flux at any energies over the bandpass used here for any of the pulse phase bins. All phase bins have net count rates (after any pileup correction) of $380\text{--}480 \text{ counts s}^{-1}$, and each bin has a net exposure of 4250 s. Further details about the individual phase bins are given in Table 1.

The reduced spectra were binned to oversample the instrumental EPIC pn spectral resolution by at most a factor of 3, and to at least 25 counts per bin, using the SPECGROUP routine. The full energy range used is 0.5–10 keV. At these high photon fluxes, EPIC pn suffers from a gain-shift issue, which is described specifically for Her X-1 in Appendix A of

Kosec et al. (2022), and more generally by Duro et al. (2016). Our mitigation strategy for this gain shift follows our approach in Kosec et al. (2022) and is also described in Section 5.

Finally, all the reduced spectra were converted from OGIP format into SPEX format using the TRAFO routine. We used SPEX (Kaastra et al. 1996) v3.07 to fit X-ray spectra and used the Cash statistic (Cash 1979) for analysis. The use of the Cash statistic is not formally necessary for any of our EPIC pn data analysis (where the number of counts per bin is very high), but it is appropriate for XRISM data simulation analysis. All uncertainties are quoted at 1σ significance.

5. Spectral Modeling and Results

After the pulse-resolved spectra are prepared, we proceed with spectral modeling to determine how the disk wind properties vary over the pulsation cycle. Her X-1 shows strong variability in the 0.5–10 keV EPIC pn energy band over the X-ray pulsation period, both in the overall count rate and in the spectral shape. We show the spectra of a number of pulse phase bins in Figure 11 in Appendix B. In particular, we notice that the hard X-rays (primarily direct emission) pulsate with a phase shift compared with the soft X-rays (primarily the reprocessing of direct emission). This effect is well known and was previously studied by Zane et al. (2004) and Brumback et al. (2021).

5.1. Spectral Model Setup

We use a simplified spectral model from Kosec et al. (2022) to fit the Her X-1 continuum and emission components in the EPIC pn energy range. Initially, we use the full 0.5–10 keV range of EPIC pn to constrain the Her X-1 spectral shape. A COMT component (Titarchuk 1994) is used to describe the hard Comptonization continuum originating from the accretion column of the neutron star. A soft blackbody with a temperature of about 0.1 keV describes the thermal reprocessing signature (Hickox et al. 2004) observed at soft X-rays (<1 keV). Additionally, we use a Gaussian line to describe the broad “1 keV” feature (e.g., Fürst et al. 2013; Kosec et al. 2022) in the soft band. The Fe K band around 6.4 keV is very complex in Her X-1—following the results of Kosec et al. (2022), we describe it using three Gaussian lines of different line widths: a narrow Gaussian (low-ionization Fe emission) with an FWHM of 0.05 keV (fixed) and an energy of 6.4 keV (fixed); a medium-width Gaussian (Fe XXV emission) with a width of about 0.5 keV (free) and an energy of 6.67 keV (fixed); and a broad Gaussian line (Fe K emission, unknown ionization state) with an energy of about 6.5 keV (free) and a width of about 2 keV (free).

All of the emission components are absorbed by the ionized disk wind plasma, the modeling of which is discussed further below. On top of this absorption, we apply Galactic absorption using the HOT model, with the absorption column density fixed to $1 \times 10^{20} \text{ cm}^{-2}$ (Kosec et al. 2022). This model describes an almost neutral absorber with a temperature of 8×10^{-6} keV (de Plaa et al. 2004; Steenbrugge et al. 2005).

Finally, to correct for the gain-shift issue in EPIC pn mentioned in Section 4, on top of all the previous spectral models, we apply a multiplicative shift model REDS that blueshifts all the spectral models by a certain factor (a free variable of the spectral fit) and thus introduces a variable gain shift to the spectral model, to match with that of the EPIC pn

data. Further details about this gain-shift correction can be found in Appendix A of Kosec et al. (2022). The value of the gain-shift parameter is anchored in the EPIC pn data by the fixed energies of certain Fe emission lines (low-ionization Fe and Fe XXV) and by the positions of the disk wind absorption lines (Fe XXV and Fe XXVI). The projected velocity of the wind ($600 \pm 40 \text{ km s}^{-1}$) was accurately measured in previous time-averaged analysis of this observation using both EPIC pn and RGS data (Kosec et al. 2023a) and so the energies of the Fe XXV and XXVI lines are known. Outside of the Fe K region, this gain correction may not be completely accurate, since applying a simple blueshift parameter may not completely describe the true EPIC pn gain-shift function. However, outside of this region, our spectral model in the 2–10 keV band is primarily just a simple, featureless power-law shape, which does not require a perfect understanding of the gain function.

The disk wind produces strong absorption lines in both the Fe K band (Fe XXV and Fe XXVI) and in the soft-X-ray band (N VII, O VIII, and Ne X). The soft-X-ray absorption is well resolved in the RGS spectra (Kosec et al. 2020, 2023a), but it is completely unresolved in EPIC pn, which has a spectral resolution of ~ 100 eV throughout the 0.5–10 keV bandpass. At the same time, the soft-X-ray band is very complex in Her X-1, containing an array of both narrow and broad emission lines in addition to wind absorption (Kosec et al. 2022). For these reasons, we only use the soft-X-ray (<2 keV) EPIC pn data to initially describe the broadband continuum and constrain the X-ray SED of Her X-1. An accurate description of the SED is necessary for photoionization modeling of the disk wind. After the soft-X-ray shape is reasonably constrained, we ignore the EPIC pn data below 2 keV, fix any spectral parameters relevant to this band (the soft blackbody, 1 keV line properties, and the seed temperature of the Comptonization component), and refit the resulting 2–10 keV spectra. With this approach, any unresolved features below 2 keV (disk wind absorption and any emission lines) will not sway our spectral fit of disk wind absorption in the crucial Fe K band.

We describe the wind absorption features in the Fe K band and study the response of the wind to X-ray pulsation using two methods: first with a phenomenological approach, where we measure the column density in the Fe XXV and XXVI ions, and second with a physical photoionization model, which allows us to measure the plasma ionization parameter $\log(\xi / \text{erg cm s}^{-1})$. We will compare whether these two methods yield consistent results.

Before proceeding to the spectral fitting, we consider the results of the time-averaged analysis of the full observation 865440101 (the same observation as used in this work), which was performed by Kosec et al. (2023a). In that work, the RGS and EPIC pn data from this observation were fitted (without performing any pulse-resolved extraction) with the photoionization model PION (see further details about this model below) and the full continuum model from Kosec et al. (2022). This is the highest-fidelity measurement of the parameters of the disk wind in Her X-1, thanks to the excellent S/N of this (full) observation and the simultaneous usage of both RGS and EPIC pn data. The pulse-resolved analysis is likely going to be more limited, as the S/N of the original observation is split into 10 pulse phase bins, and importantly we are unable to use the simultaneous RGS spectra, since the frame time of the RGS instrument (in standard spectroscopy mode) is longer than the pulse period of Her X-1.

Table 2
Best-fitting Disk Wind Properties from the Phenomenological and Physical Analysis of EPIC pn Data from Observation 0865440101

Pulse Bin	Time (s)	0.5–10 keV Luminosity (10^{36} erg s $^{-1}$)	SLAB Model		PION Model		
			log Fe XXV Column Density ^a (cm $^{-2}$)	log Fe XXVI Column Density ^a (cm $^{-2}$)	log(ξ /erg cm s $^{-1}$)	log Fe XXV Column Density (cm $^{-2}$)	log Fe XXVI Column Density (cm $^{-2}$)
0	0	10.2 $^{+0.09}_{-0.10}$	17.36 $^{+0.44}_{-0.47}$	18.51 $^{+0.14}_{-0.12}$	3.55 $^{+0.10}_{-0.09}$	17.43 $^{+0.21}_{-0.24}$	18.29 $^{+0.08}_{-0.10}$
1	0.124	7.65 $^{+0.14}_{-0.14}$	17.54 $^{+0.33}_{-0.35}$	18.27 $^{+0.19}_{-0.23}$	3.56 $^{+0.12}_{-0.10}$	17.30 $^{+0.23}_{-0.32}$	18.23 $^{+0.09}_{-0.14}$
2	0.248	7.29 $^{+0.28}_{-0.41}$	16.95 $^{+0.52}_{-3.95}$	18.22 $^{+0.20}_{-0.20}$	3.68 $^{+0.14}_{-0.12}$	16.94 $^{+0.33}_{-0.41}$	18.08 $^{+0.15}_{-0.19}$
3	0.371	6.65 $^{+0.56}_{-0.72}$	16.1 $^{+1.2}_{-3.1}$	18.11 $^{+0.17}_{-0.19}$	3.64 $^{+0.21}_{-0.17}$	16.85 $^{+0.46}_{-0.60}$	18.04 $^{+0.20}_{-0.29}$
4	0.495	5.83 $^{+0.54}_{-0.52}$	<16.75	18.07 $^{+0.14}_{-0.14}$	3.58 $^{+0.15}_{-0.15}$	16.86 $^{+0.44}_{-0.42}$	18.03 $^{+0.19}_{-0.20}$
5	0.619	8.51 $^{+0.09}_{-0.09}$	16.53 $^{+0.80}_{-3.54}$	18.25 $^{+0.21}_{-0.21}$	3.98 $^{+0.15}_{-0.12}$	16.64 $^{+0.32}_{-0.41}$	17.95 $^{+0.15}_{-0.19}$
6	0.743	13.9 $^{+0.10}_{-0.12}$	17.32 $^{+0.50}_{-1.01}$	17.76 $^{+0.23}_{-0.15}$	4.12 $^{+0.11}_{-0.12}$	16.13 $^{+0.33}_{-0.30}$	17.71 $^{+0.16}_{-0.15}$
7	0.867	15.8 $^{+0.20}_{-0.19}$	16.1 $^{+0.86}_{-3.1}$	17.85 $^{+0.15}_{-0.15}$	3.84 $^{+0.11}_{-0.10}$	16.42 $^{+0.27}_{-0.31}$	17.84 $^{+0.13}_{-0.15}$
8	0.990	13.6 $^{+0.51}_{-0.29}$	17.22 $^{+0.44}_{-4.22}$	17.78 $^{+0.14}_{-0.17}$	3.86 $^{+0.10}_{-0.11}$	16.33 $^{+0.32}_{-0.29}$	17.81 $^{+0.15}_{-0.14}$
9	1.114	12.9 $^{+0.08}_{-0.10}$	<16.64	17.87 $^{+0.10}_{-0.10}$	3.89 $^{+0.07}_{-0.12}$	16.60 $^{+0.32}_{-0.21}$	17.93 $^{+0.15}_{-0.10}$

Notes. The 0.5–10 keV luminosity is calculated from the observed X-ray flux after accounting for disk wind and Galactic absorption.

^a We imposed a lower limit of 13 for the $\log(N_{\text{H}}/\text{cm}^{-2})$ of the Fe XXV and Fe XXVI column density.

The time-averaged analysis allowed Kosec et al. (2023a) to determine the following wind photoionization properties: a column density of $1.00^{+0.09}_{-0.05} \times 10^{23}$ cm $^{-2}$, an ionization parameter $\log(\xi/\text{erg cm s}^{-1})$ of $3.77^{+0.03}_{-0.02}$, a velocity width of 186 ± 15 km s $^{-1}$, and a systematic velocity of -600 ± 40 km s $^{-1}$ (here given uncorrected for the Her X-1 orbital motion). At such high-ionization parameters, the huge majority of the Fe K wind absorption will be in the Fe XXV and Fe XXVI transitions, and in the 2–10 keV energy band the ratio of these two transitions will be the driver for the ionization parameter measurement.

Finally, in order to compare the pulse-resolved disk wind properties with the X-ray pulsations of Her X-1, as well as for the TPHO simulations (Section 3), we calculated the 0.5–10 keV unabsorbed luminosity for each pulse phase bin during the physical photoionization modeling analysis, using the best-fitting X-ray continuum.

5.2. Phenomenological Disk Wind Modeling

The first pulse-resolved modeling approach is phenomenological and we apply the SLAB model (Kaastra et al. 2002) within SPEX to describe the disk wind features. SLAB calculates the transmission through a slab of plasma, where all ionic column densities are allowed to vary independently and are only tied by a common systematic velocity, line velocity width, and the covering fraction. This model gives us an opportunity to measure the column densities only in certain ions, which are less prone to full-energy-band spectral behavior (e.g., SED variations) and therefore systematic uncertainties in the more complex photoionization models. We use SLAB to determine the wind column density in the Fe XXV and Fe XXVI ions for each pulse phase bin, in order to probe how they respond to changes in the illuminating X-ray continuum. We fix the outflow velocity and the velocity width of the component to the values obtained from the time-averaged photoionization analysis. These quantities are very unlikely to vary systematically over the (very short) pulse period, because the orbital period of particles within the outflow is not related to the neutron star rotation period (the outflow is located far beyond the neutron star magnetosphere).

The constraints on the Fe XXV ion column density are generally quite loose and hard to interpret in terms of X-ray pulsation, as the ion is significantly detected only in a few pulse phase bins. The measurements are listed in Table 2. On the other hand, the Fe XXVI ion column density is well measured in all of the 10 phase bins and it shows a very clear anticorrelation with the 0.5–10 keV Her X-1 luminosity. The results are shown in Table 2 as well as in Figure 4, where the column density in the Fe XXVI ion is plotted versus the pulse phase bin number. The same figure also contains the Her X-1 0.5–10 keV unabsorbed luminosity for each phase bin (in red). We observe that while the $\log(N_{\text{H}}/\text{cm}^{-2})$ of the Fe XXVI column density is around 18.1–18.2 when the X-ray luminosity is low, it significantly decreases when the X-ray luminosity increases, down to about $\log(N_{\text{H}}/\text{cm}^{-2}) \sim 17.8$. In other words, some of the Fe XXVI state atoms are fully ionized when the observed X-ray luminosity rapidly increases and the plasma ionization rises in response (see Figure 12 in Appendix C), but recombine again into Fe XXVI when the X-ray luminosity returns to the original value. These results can be directly compared with the TPHO simulations from Section 3, shown in Figure 2. The very quick response of the plasma to variations in the X-ray luminosity on 1 s timescales, with no obvious time delays, indicates that the plasma density is high, at least 10^{12} cm $^{-3}$.

5.3. Physical Photoionization Disk Wind Modeling

As a second approach, we use the photoionization spectral model PION to describe the disk wind features. PION (Miller et al. 2015; Mehdipour et al. 2016) calculates the transmission through a slab of plasma by self-consistently determining the ionizing balance using the SED of the currently loaded continuum model. It is therefore one of the highest-fidelity currently available physical photoionization models. Practically, the SED shape and luminosity used by PION will contain some extrapolation of the models we are using to describe the Her X-1 continuum (particularly the hard Comptonization and the soft blackbody) beyond the available 0.5–10 keV band of EPIC pn. This is one of the drawbacks of the photoionization wind analysis, given our data set with a limited energy range.

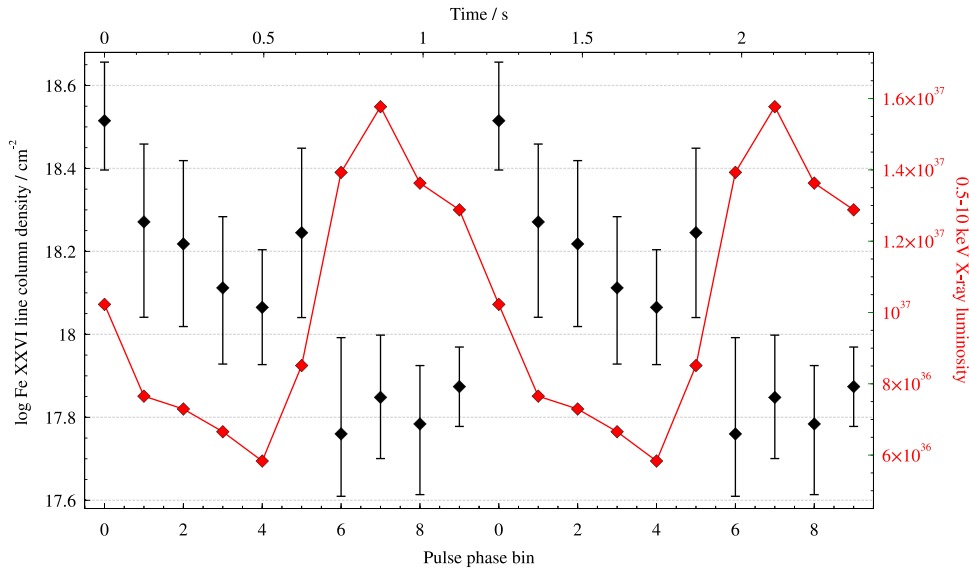


Figure 4. Fe XXVI ion column density of the Her X-1 disk wind (black points) vs. the pulse phase bin (on the bottom X-axis) and vs. time (on the top X-axis). In the red color, we show the 0.5–10 keV unabsorbed Her X-1 luminosity vs. the phase bin and time. The Fe XXVI ions respond to the variation in X-ray luminosity over the pulsation period.

PION assumes photoionization equilibrium of wind plasma for each pulse phase bin, which may not be a correct assumption. However, at these precession phases (0.02–0.04), the wind number density is expected to be reasonably high, and so the plasma should not be too far from the equilibrium. Even if that was not the case, the ionization parameter, which in these fits is determined primarily from the ratio of the Fe XXV and XXVI transitions, would still offer a very good guideline as to the immediate ionization state of the wind. As discussed in Section 3, we prefer not to directly fit the observed spectra with the time-dependent photoionization model TPHO due to the constant SED approximation in the current version of TPHO.

We use the PION model to determine the ionization parameter $\log(\xi/\text{erg cm s}^{-1})$ of the disk wind at each phase bin. The column density, outflow velocity, and velocity width parameters are fixed to the best-fitting values from the time-averaged fit of this observation, as they are unlikely to vary in a correlated way over the pulsation period. We also adopt the best-fitting wind elemental abundances from Kosec et al. (2023a), which are $(\text{N}/\text{O})=3.4_{-0.8}^{+0.6}$, $(\text{Ne}/\text{O})=2.3_{-0.5}^{+0.4}$, and $(\text{Fe}/\text{O})=2.1 \pm 0.3$.

We note that we encountered an issue while fitting pulse phase bin number 8, where a very low $\log(\xi/\text{erg cm s}^{-1})=3.26_{-0.10}^{+0.11}$ was obtained initially. Our interpretation is that this issue occurred because of an incorrect extrapolation of the Her X-1 SED shape above 10 keV (beyond the EPIC pn energy band). The model originally fitted the (extrapolated) 0.1–100 keV Her X-1 luminosity to be a factor of 10 higher than that of the two neighboring phase bins. From hard-X-ray pulse-resolved X-ray studies (e.g., Fürst et al. 2013), we know that such a large X-ray luminosity cannot be correct. Specifically, this is likely an issue with the hard Comptonization model COMT—but it is not a technical issue. Apparently, the Her X-1 continuum during phase bin 8 decreases faster beyond 10 keV than predicted by COMT. We used an extra exponential cutoff model (ETAU in SPEX) to adjust the calculated 0.1–100 keV luminosity of bin 8 to be the average of the two neighboring bins (7 and 9). Doing so increased the best-fitting ionization parameter to $\log(\xi/\text{erg cm s}^{-1})=$

$3.86_{-0.11}^{+0.10}$. We note that none of the remaining pulse phase bins had an abnormal extrapolated 0.1–100 keV luminosity. Nevertheless, this issue underlines the need for good coverage of the full X-ray band where Her X-1 peaks (0.3–50 keV) in future studies. Unfortunately, no simultaneous NuSTAR data are available for XMM-Newton observation 865440101.

The best-fitting ionization parameter $\log(\xi/\text{erg cm s}^{-1})$ is shown in Figure 5 versus the pulse phase bin number, alongside the 0.5–10 keV luminosity. For comparison with the phenomenological fitting approach, we used the ASCDUMP command in SPEX to determine the column densities of the Fe XXV and XXVI ions in the PION model. All these measurements are given in Table 2.

A response of the ionized wind to the X-ray pulsation is clear—the pulse phase bins with higher 0.5–10 keV luminosity show consistently higher ionization parameters. Again, comparing with the TPHO simulations, we conclude that the wind number density must be at least 10^{12} cm^{-3} for such a quick response, confirming our time-averaged ionization state modeling results. The Fe XXVI column density is anticorrelated with the ionization parameter (as it should be; see Figure 12) and in good agreement with the phenomenological wind modeling for most phase bins. The exception is phase bin 5, where the 0.5–10 keV luminosity is beginning to rise slightly. The Fe XXVI column density still remains relatively high, but in the photoionization analysis, the ionization parameter has already significantly increased. We could not find the cause of this discrepancy, but it could again be related to the underlying PION modeling of the SED from the extrapolated Her X-1 continuum model.

6. XRISM Simulations

In the previous section, we showed that the highest-quality XMM-Newton observation of the disk wind in Her X-1 allows us to directly detect the variation of its ionization properties over the pulsation period. Lower-quality wind observations (with shorter exposure times) at low Her X-1 precession phases, when the wind signatures are strong, may also be sufficient to detect this variation (at lower significance).

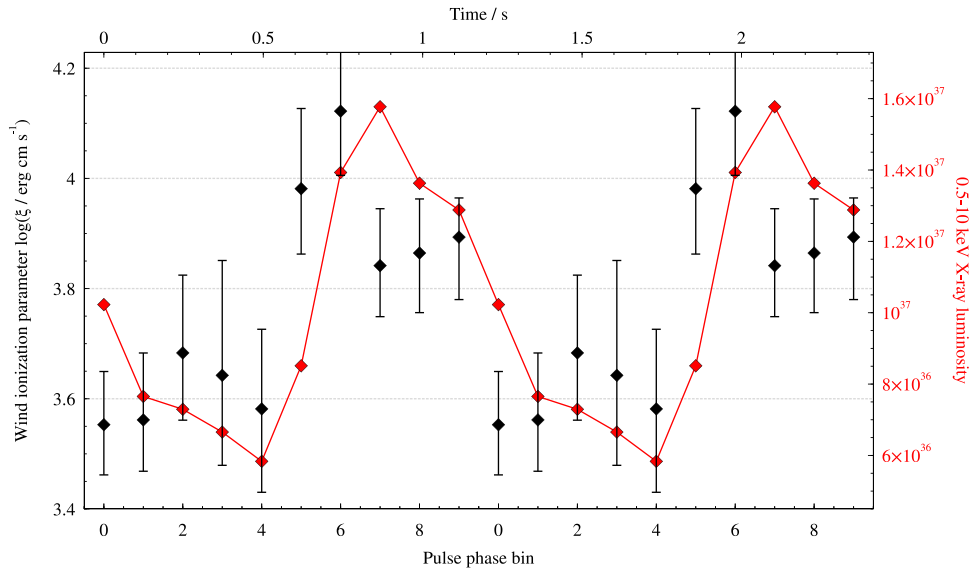


Figure 5. Disk wind ionization parameter $\log(\xi/\text{erg cm s}^{-1})$ (black points) vs. the pulse phase bin (on the bottom X-axis) and vs. time (on the top X-axis). In the red color, we show the 0.5–10 keV unabsorbed Her X-1 luminosity vs. the pulse phase bin and time. Significant variation of the ionization parameter is observed over the pulsation period, as the wind ionization state responds to the X-ray variation.

However, the wind absorption significantly weakens with increasing precession phase (Kosec et al. 2023a) and so its variation over the pulsation period is unlikely to be detectable with current X-ray instruments—such as EPIC pn on board XMM-Newton, NICER, or Chandra—at higher precession phases.

In 2023 September, a new high-resolution X-ray spectroscopy mission, XRISM (XRISM Science Team 2020), was launched. XRISM offers excellent spectral resolution of about 5 eV across the 0.5–10 keV band thanks to its Resolve microcalorimeter instrument. XRISM is therefore perfect for spectroscopic observations of the Fe K band, which in Her X-1 contains the important Fe XXV and XXVI wind absorption lines. These transitions are crucial for the determination of the outflow ionization state. Second, XRISM offers a very good effective area for a high-resolution instrument. Figure 6 of Kosec et al. (2023b) shows a simulated spectrum from a 10 ks exposure XRISM observation of Her X-1 in the short high state, focusing on the Fe K band. The data quality of this very brief exposure simulation in the short high state (which is a factor of 2–3 fainter than the main high state) is excellent, and the disk wind absorption lines are easily spectrally resolved. Even shorter exposures will be sufficient to accurately measure the ionization properties of the outflow of Her X-1. Finally, the Resolve microcalorimeter offers very good time resolution of less than 1 ms.

We perform XRISM simulations in order to determine the performance of this instrument and to understand if its future observations will allow us to directly measure the plasma number density in the outflow of Her X-1, for which we can currently only obtain lower limits. We use publicly available XRISM simulation responses⁹ and assume that the goal of 5 eV spectral resolution will be achieved. We also note that we assume the gate-valve-open configuration of the Resolve instrument. Since the disk wind lines that are the most important for the ionization parameter measurement, Fe XXV and XXVI, are located in the Fe K band, a closed gate valve

does not mean that XRISM cannot perform this science. However, the exposure needs to be increased accordingly (by about 60%) to reach the quality of results in these simulations.

As in Section 3, we perform spectral simulations using the time-dependent photoionization model TPHO. As the X-ray pulsation light curve, we again choose the 0.5–10 keV unabsorbed light curve from observation 0865440101. The underlying emission continuum is the best-fitting Her X-1 continuum from that observation, but scaled by the 0.5–10 keV light curve in each of the 10 pulse phase bins (each of the individual spectral components is scaled by the same factor). This way, we ensure a constant shape of the continuum SED, as required by the current version of TPHO.

We probe the detectability of the wind response to X-ray pulsation with XRISM for different precession phases of Her X-1. Therefore, we test a number of different wind properties (column densities and ionization parameters). We use the representative wind properties determined in Appendix A for the precession phases of 0.03, 0.06, 0.09, and 0.13. Finally, we test a broad range of possible wind number densities, following Section 3: from very low (10^{10} cm^{-3}) to high (10^{14} cm^{-3}) densities.

In the real observations of Her X-1 with XRISM throughout the precession phase, the underlying time-averaged as well as pulse-resolved emission continuum of the source is bound to evolve. However, this is unlikely to introduce significant extra uncertainties on the recovered wind properties, as the overall time-averaged continuum flux does not significantly change throughout the main high state and the wind absorption lines are narrow and easily separable from the spectral continuum at the excellent XRISM resolution.

Following the approach discussed in Section 3, we introduce the TPHO wind absorption component and evolve the plasma for five full pulsation cycles, to obtain a stable ionization response. Afterward, we simulate XRISM spectra for 10 pulse phase bins over the rotation period of Her X-1. We mimic a 25 ks total exposure XRISM observation by simulating 10 2.5 ks exposure phase bins. The mock XRISM spectra are saved individually, and each of them is fitted using the PION

⁹ <https://heasarc.gsfc.nasa.gov/docs/xrism/proposals/>

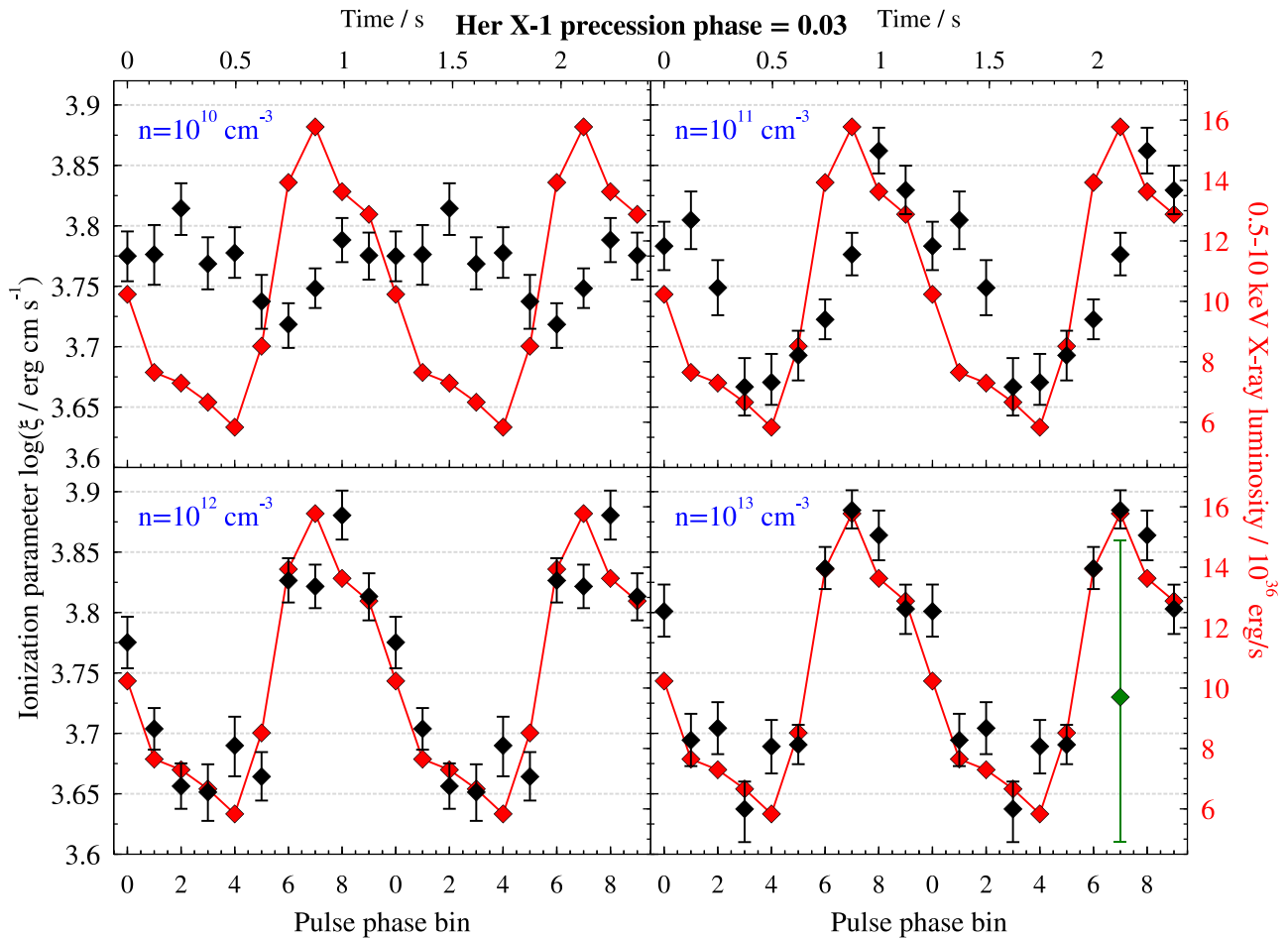


Figure 6. Pulse-resolved analysis (10 bins per pulsation period) of simulated 25 ks XRISM observations of Her X-1 at a precession phase of 0.03 (column density 10^{23} cm^{-3} , $\log(\xi/\text{erg cm s}^{-1})$ of 3.77). The different panels show simulations with different input plasma number densities. The red diamonds show the underlying X-ray pulsation light curve, and the black diamonds show the best-fitting ionization parameter $\log(\xi/\text{erg cm s}^{-1})$ for each simulated XRISM pulse phase bin. For comparison, the green data point in the bottom right panel shows the mean uncertainty on the $\log(\xi/\text{erg cm s}^{-1})$ measurement from the analysis of XMM-Newton observation 0865440101 (Section 5).

photoionization model, to determine the best-fitting immediate ionization parameter of the wind plasma. This procedure is followed for all simulated wind number densities and for XRISM simulations at all the different Her X-1 precession phases.

The results for the simulated XRISM observation at a precession phase of 0.03 are shown in Figure 6. The figure is composed of four panels corresponding to different input plasma number densities (10^{10} through 10^{13} cm^{-3}). Each panel is similar to Figure 5, but instead of EPIC pn data, it contains a 25 ks XRISM observation simulation. We conclude that XRISM can easily and significantly detect any plasma ionization variations in the simulated exposure. For very low number densities (10^{10} cm^{-3}), the outflow response is very weak, as expected. At higher densities (10^{11} cm^{-3}), the response is stronger, but very delayed. At high densities (10^{12} and 10^{13} cm^{-3}), the response is fast and strong. We also simulated XRISM spectra for a plasma number density of 10^{14} cm^{-3} , but did not find significant visual differences with the results from those at a number density of 10^{13} cm^{-3} . Even though no differences may be seen visually, direct fitting with a future version of the TPHO model (incorporating a variable SED) will likely place strong constraints on the plasma number density. Even in the worst case, it will result in a significantly

more constraining number density lower limit than the XMM-Newton observations.

As the XRISM data have excellent spectral resolution and the wind absorption is strong at the precession phase of 0.03, the uncertainties on the simulated data points are very small. The mean uncertainties on the ionization parameter are about $\Delta\log(\xi/\text{erg cm s}^{-1}) \sim 0.02$, whereas in the XMM-Newton PION analysis (Section 5), they were on average $\Delta\log(\xi/\text{erg cm s}^{-1}) \sim 0.12$. To show this visually, we added the mean XMM-Newton $\log(\xi/\text{erg cm s}^{-1})$ uncertainty in the bottom right panel of Figure 6.

We also performed XRISM simulations for wind properties at precession phases of 0.06 and 0.09. The results are shown in Figures 7 and 8. The wind absorption is weaker in comparison with phase ~ 0.03 , since the column density is lower, but the response of the plasma to X-ray pulsation is still detectable in a 25 ks exposure.

Finally, we perform a 25 ks simulation for wind properties equivalent to a precession phase of 0.13. Here, the wind absorption is so weak that the response is no longer detectable with XRISM using 10 pulse phase bins. The outflow is still significantly detected in the time-averaged 25 ks spectrum, and so a coarser pulse-resolved analysis (e.g., with five bins per

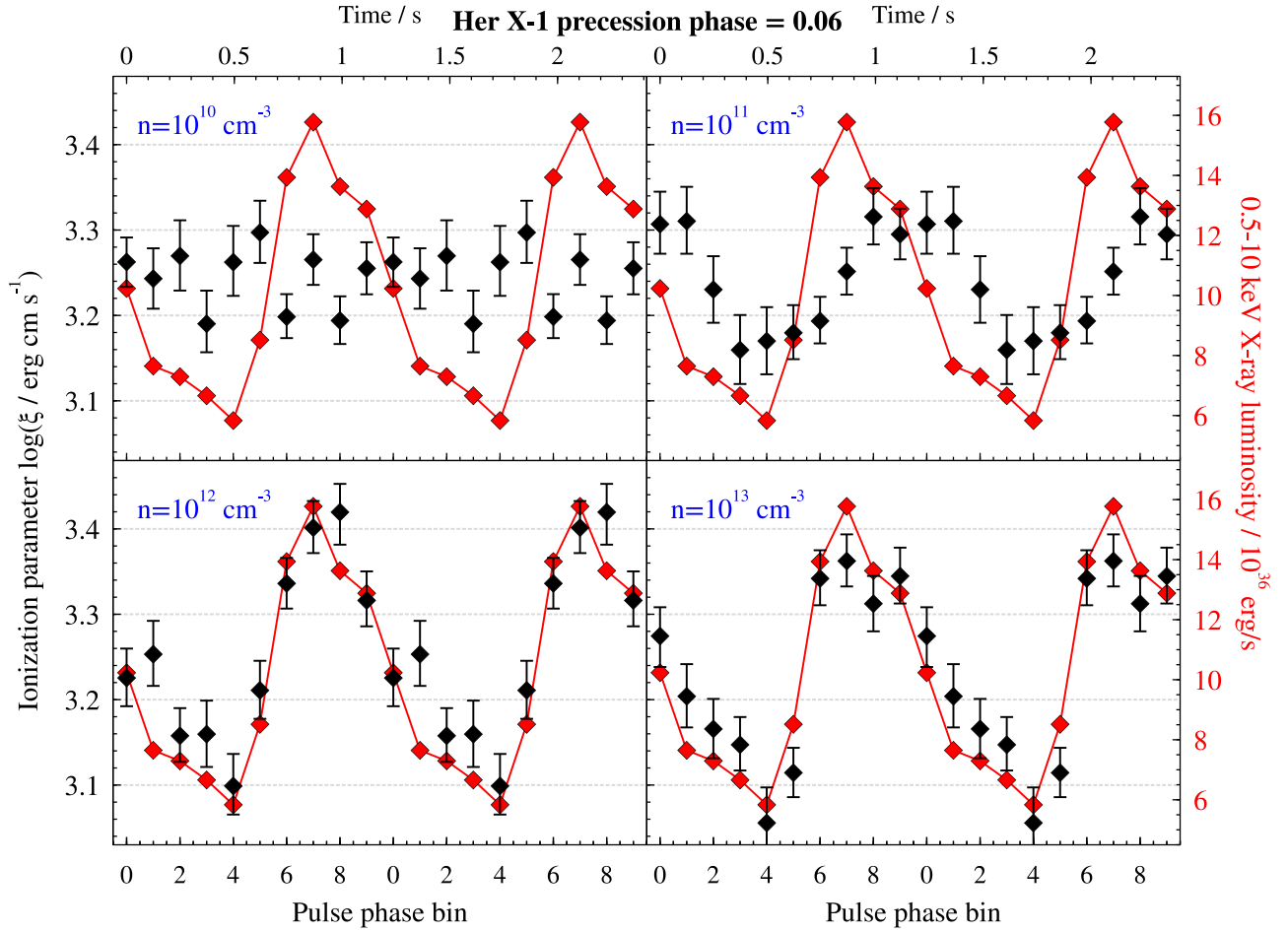


Figure 7. The same as Figure 6, but for representative disk wind properties of Her X-1 at the precession phase of 0.06 (column density 10^{22} cm^{-3} , $\log(\xi/\text{erg cm s}^{-1})$ of 3.25).

pulse period) may still be capable of detecting the wind response, provided the number density is sufficient.

7. Discussion

We study the ionization response of the accretion disk wind in Her X-1 to the X-ray pulsations at the neutron star rotation frequency. We find that given the number density limits derived from previous wind spectroscopic observations, the response can be sufficiently fast to be detected in X-ray observations. We then perform a pulse-resolved analysis of the best-quality XMM-Newton observation of the Her X-1 disk wind and detect this ionization response.

We use two different spectral modeling approaches to measure how the ionization state of the wind responds to the X-ray pulsations in the best-quality Her X-1 disk wind observation (0865440101). In the first method, we track the pulse-resolved evolution of individual ion column densities (Fe XXV and XXVI). Second, we track the ionization parameter $\log(\xi/\text{erg cm s}^{-1})$ of the disk wind plasma using the physical photoionization model PION. The phenomenological analysis shows that the Fe XXVI column density sharply drops just as the X-ray flux increases (and some of the Fe XXVI ions are fully ionized), and returns back to the high value when the X-ray flux reduces. The Fe XXV ion is detected only weakly throughout the pulse period, but its column density evolution agrees with the Fe XXVI results. The ionization parameter

evolution in the PION physical analysis is broadly consistent with the phenomenological results, despite one inconsistency, which may be due to the measurement of the underlying X-ray illumination SED (which must be extrapolated from the available 0.5–10 keV energy band). At these high ionization levels, the PION model determines the $\log(\xi/\text{erg cm s}^{-1})$ parameter primarily from the strengths of the Fe XXV and XXVI lines. We observe good agreement between the column densities of these Fe ions as predicted by PION and measured by the SLAB model (Table 2).

Unfortunately, during XMM-Newton observation 0865440101, there was no simultaneous observation with the NuSTAR X-ray telescope, which would have been able to capture the hard-X-ray SED of Her X-1 up to 79 keV. Additionally, we are unable to use the simultaneous RGS grating spectra for the pulse-resolved analysis, as the instrument was operated in normal spectroscopy mode during the observation, which has a frame time much longer than the 1.24 s X-ray pulsation period. With RGS data, we would have been able to significantly decrease the uncertainties on the $\log(\xi/\text{erg cm s}^{-1})$ measurements as well as measure the column densities in other strong disk wind ions, such as O VIII and Ne X.

Both the phenomenological and physical modeling methods indicate a fast response of the disk wind to X-ray pulsations, and we do not detect any clear delay in this response. Comparing this with the TPFO simulations (Figure 2), the EPIC

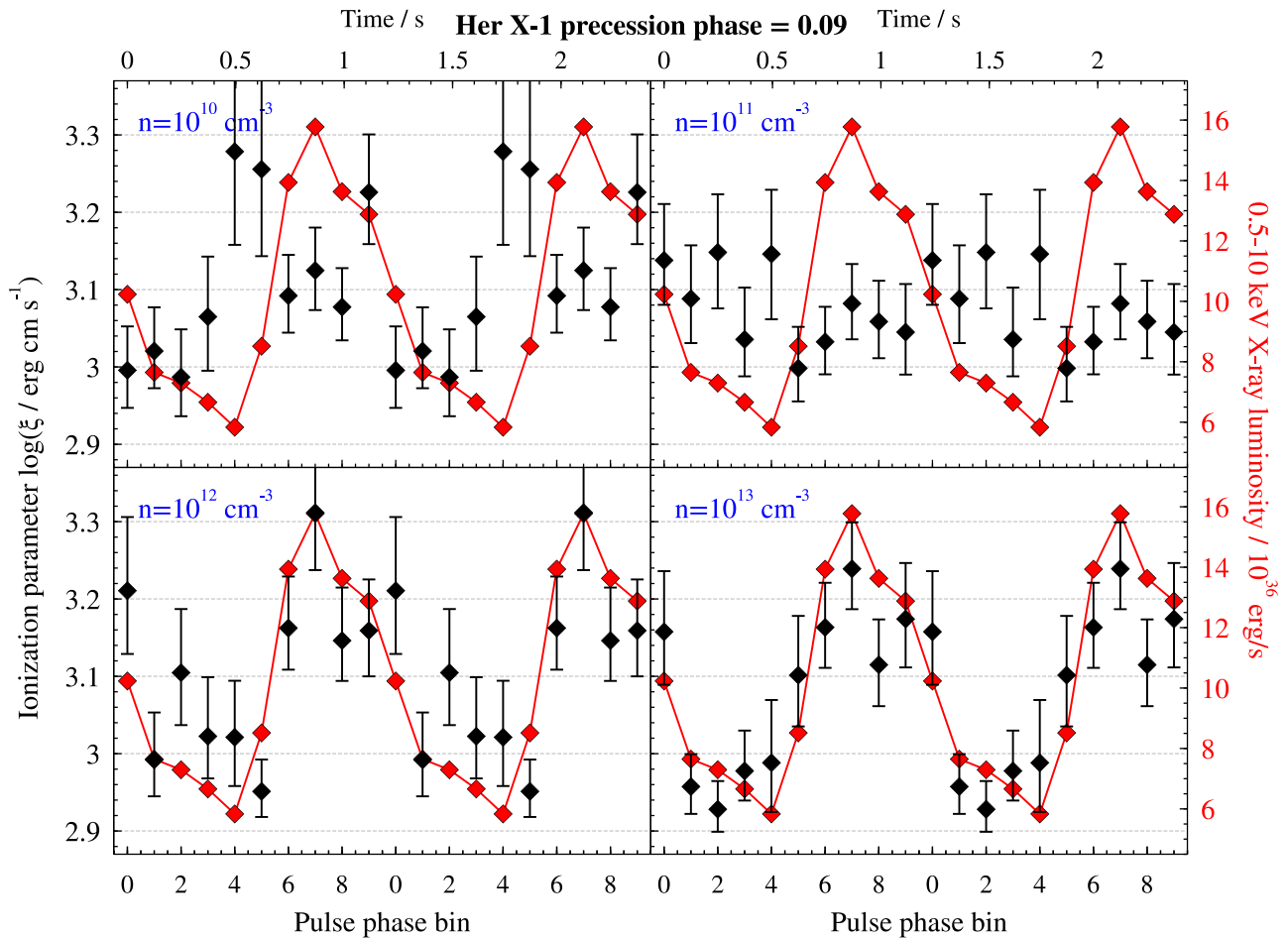


Figure 8. The same as Figure 6, but for representative disk wind properties of Her X-1 at the precession phase of 0.09 (column density $3 \times 10^{21} \text{ cm}^{-3}$, $\log(\xi/\text{erg cm s}^{-1})$ of 3.1).

pn results suggest that the wind number density must be significantly higher than 10^{11} cm^{-3} , most likely at least 10^{12} cm^{-3} . This is a completely independent confirmation of the lower limit on density obtained from the time-averaged wind spectroscopic analysis, which indicates that $n \gtrsim 4 \times 10^{12} \text{ cm}^{-3}$.

The best-quality XMM-Newton EPIC pn data set shows variations in the ionization state of the wind at high statistical significance, despite the complexity of the Fe K region in Her X-1, thanks to its long exposure and the strength of the ionized absorption from the wind at this precession phase. At higher precession phases, when the wind absorption is weaker, the effect is likely undetectable with XMM-Newton.

Chandra HETG gratings (Canizares et al. 2005) offer better spectral resolution than EPIC pn in the Fe K band, but also a poorer effective area, requiring more exposure time. In the continuous clocking (CC) mode (3 ms timing resolution), they are capable of detecting the wind time variation over the pulsation period, but again only when the wind absorption is strong. HETG spectra in the CC mode were previously used to perform a phase-resolved analysis of disk wind absorption during the heartbeat state of the black hole X-ray binary GRS 1915+105 (Nielsen et al. 2011). The heartbeats of GRS 1915 are quasiperiodic, with a typical duration of about 50 s. With the phase-resolved analysis, Nielsen et al. (2011) detected variations in the Fe XXV/Fe XXVI absorption-line properties on timescales as short as 5 s.

We conclude that with the current X-ray instruments, we can set a lower limit on the wind number density at low precession phases (low heights above the accretion disk), but cannot directly measure its value. At greater heights above the disk, we are likely unable to place any relevant constraints on the wind number density via time-dependent photoionization modeling. However, in order to significantly constrain the wind mass outflow rate, energetics, and launching mechanism, we ideally need multiple number density measurements (or strong constraints) at different locations within the outflow.

In Section 6, we find that the best instrument for pursuing an accurate wind number density measurement throughout the outflow is the recently launched XRISM telescope, which combines excellent spectral resolution with a very good effective area in the Fe K band. Our XRISM simulations of the Her X-1 disk wind response to X-ray pulsation show that this effect is detectable throughout a significant fraction of the main high state of Her X-1 (at least up to and including the precession phase of 0.09). At very low phases, the wind number density must be high ($n \gtrsim 4 \times 10^{12} \text{ cm}^{-3}$) and so the wind response is very fast. Even with XRISM, it may only be possible to obtain a lower limit to the wind density. In any case, thanks to the superior XRISM data quality, the limit is likely going to be more informative than the one from XMM-Newton data. At higher precession phases that sample greater heights along the wind streamlines, unless the wind clumps up very quickly, the number density will most likely decrease.

Therefore, the wind response to pulsations should become progressively slower. If the density drops below about 10^{12} cm^{-3} , this change will be directly (and accurately) measurable with XRISM. At even higher phases, the density may drop to such low values that the wind would no longer be capable of any response to the X-ray pulsations.

To sum up, XRISM observations at low precession phases will put at least a lower limit on the wind density, while observations at greater phases will most likely be capable of directly measuring the density value. Finally, observations at the highest phases may even put upper limits on the wind density, based on the lack of any response, while the photoionization balance analysis will still place a lower limit on the density. Therefore, a coordinated observational campaign on Her X-1 with XRISM, sampling its disk wind properties throughout a significant fraction of the main high state, will allow us to measure the number density of the wind at multiple locations and heights above the disk. This accurate measurement of the number density and the wind properties (in 2D) will constrain the total mass outflow rate and energetics, enabling us to infer the outflow launching mechanism and the impact it has on the X-ray binary system and its surroundings.

Our analysis of the 0.5–10 keV XMM-Newton spectra highlights the need to accurately constrain the pulse-resolved SED of Her X-1 to model the disk wind variation correctly. XRISM, with a useful energy range from 0.3 keV up to about 17 keV, will be able to place better constraints on this SED shape (which peaks around 20–25 keV) than XMM-Newton. However, at least partial simultaneous coverage of any XRISM observations with a hard-X-ray observatory such as NuSTAR would still be greatly beneficial for a more robust SED determination. This would extend the visibility up to 80 keV and cover practically all of the SED of Her X-1.

7.1. Other Potential Applications of Time-dependent Photoionization Analysis in X-Ray Binaries

As shown in this study, time-dependent photoionization analysis can be a powerful tool for constraining the properties of ionized plasma and outflows in X-ray binaries exhibiting significant X-ray time variability. In many cases, the variability of these systems may be too fast to achieve a sufficient S/N for such a spectral analysis. However, the repetition of X-ray flux variations provides the crucial boost to S/N in our case of Her X-1. Such a strategy may be applied to other systems. X-ray bursts are an excellent example of strong and fast X-ray variability, but as they are very brief, the stacking of many bursts may be required to detect the ionization response of any plasma signatures in their spectra (Strohmayer et al. 2019).

Unfortunately, accretion disk winds do not appear to be common among the population of accreting X-ray pulsars that are the best candidates for this kind of analysis, as they often pulsate with a period of about 1 s. However, time-dependent photoionization modeling could potentially be leveraged to study the properties of donor star outflows in high-mass X-ray binaries such as Vela X-1 (e.g., Kretschmar et al. 2021). Assuming that the pulsation period is either much lower or much higher than the donor wind clump-crossing time and that the plasma number density is sufficiently high, the ionization response should be detectable in a high-quality X-ray data set.

Other types of objects pulsating at similar periods (~ 1 s) are the neutron-star-powered ULXs (e.g., Bachetti et al. 2014). A major issue is that they are much fainter than Galactic X-ray

binaries, due to their megaparsec distances. Second, their pulsed fraction (giving the strength of the periodic variability) is in most cases lower than the 40%–50% fraction observed in Her X-1, and only a few have shown evidence of ionized outflows to date (Kosec et al. 2018; van den Eijnden et al. 2019). An exception is NGC 300 ULX-1, a pulsating ULX that showed both an ionized outflow (Kosec et al. 2018) as well as a high-pulsed fraction (of more than 50%; Carpano et al. 2018). Observations of similar sources with future high-resolution, high-effective-area X-ray telescopes such as Athena (yielding very-high-quality spectra) would be an excellent opportunity for time-dependent photoionization studies, allowing us to improve our understanding of ULX outflows (Pinto & Kosec 2023).

The final class of objects we consider here is the accretion-powered X-ray millisecond pulsars (Wijnands 2004; Di Salvo & Sanna 2022). Their X-ray pulsations could be leveraged in a time-dependent photoionization modeling (assuming that the pulsed fraction is sufficient), and some of them show evidence for ionized outflows (Marino et al. 2022). However, their X-ray variability timescales, given the rotation periods of 100 Hz and above, may be too fast. Unless the plasma has a very high number density, it will not have sufficient time to respond to these periodic variations.

In the present study, we exclusively measure the ionization response of a disk wind through its absorption lines. In principle, a similar study can also be performed for any ionized emission lines in a time-variable X-ray binary spectrum. Such analysis is more complicated, as the ionized emission can originate in a much more spatially complex and extended region in comparison with the ionized absorption (which necessarily originates somewhere along our line sight toward the X-ray source). Additionally, it will be important to consider how the light travel time effects (which do not play a role in absorption) influence the observed line response. Nevertheless, the response of the emission lines observed in accreting pulsars to X-ray pulsation could still reveal valuable information about their origin.

In the most ideal accretion disk wind study, we would combine the time-variable responses of both the absorption and the emission from the wind, as well as use the Doppler information in the wind spectral lines. As a result, we would be able to obtain an equivalent of a Doppler tomograph (Marsh & Horne 1988; Marsh 2005), but sampled by the illumination pattern of the X-ray pulsar rather than by the orbital motion of the binary. In order to achieve this, excellent spectral resolution is required and both the absorption and the emission lines must be detected at very high statistical significance. Such analysis may be possible with XRISM or Athena (Nandra et al. 2013) observations of Her X-1.

8. Conclusions

We have performed an extensive pilot study assessing how the ionization state of the disk wind in Her X-1 responds to the periodic pulsation of the illuminating X-ray continuum, which is introduced by the neutron star rotation. We have specifically studied how this plasma state response can be used to uniquely measure the wind number density. Our findings can be summarized as follows:

1. From previous time-averaged X-ray spectroscopic observations of Her X-1, we were able to constrain the wind

number density to be between 10^9 and 10^{14} cm^{-3} throughout the main high state of Her X-1. At low precession phases (low disk wind heights above the accretion disk), the number density must be on the high end of this range ($>10^{12} \text{ cm}^{-3}$), but it can decrease to lower values of the range at higher precession phases (and greater heights above the disk).

- Based on our simulations using the time-dependent photoionization model TPHO, at low precession phases (where the wind number density is high), the ionization response of the wind to the X-ray pulsation of Her X-1 should be fast, strong, and directly detectable. At higher precession phases, the wind density can be lower, possibly resulting in a slower and weaker ionization response and, for the lowest allowed number densities, no response at all.
- By performing a pulse-resolved analysis of the best-quality XMM-Newton observation of the Her X-1 disk wind, taken at a low precession phase, we have directly detected this wind response to X-ray pulsation. Variations over the pulsation period are observed in both the Fe XXVI ion column density (using phenomenological spectral modeling) and in the wind ionization parameter (using physical photoionization modeling) with no detectable time delays, indicating a wind number density of at least 10^{12} cm^{-3} .
- We have shown that the recently launched XRISM X-ray telescope will be capable of detecting the Her X-1 wind variations over the pulsation period throughout a significant fraction of the main high state. Finally, we have discussed how a coordinated observational campaign with XRISM would allow us to accurately measure the wind number density at different points within the outflow, constraining the wind mass outflow rate, its energetics, and the launching mechanism.

Acknowledgments

Support for this work was provided by the National Aeronautics and Space Administration through the Smithsonian Astrophysical Observatory (SAO) contract SV3-73016 to MIT for Support of the Chandra X-Ray Center and Science Instruments. P.K. and E.K. acknowledge support from NASA grants 80NSSC21K0872 and DD0-21125X. Support for this work was provided by NASA through the NASA Hubble Fellowship grant HST-HF2-51534.001-A awarded by the Space Telescope Science Institute, which is operated by the Association of Universities for Research in Astronomy, Incorporated, under NASA contract NAS5-26555. C.P. acknowledges support by INAF Large Grant BLOSSOM and PRIN MUR 2022 SEAWIND.

Facilities: XMM, XRISM.

Software: SPEX (Kaastra et al. 1996), Veusz, Stringray (Huppenkothen et al. 2019a, 2019b).

Appendix A

Representative Disk Wind Properties of Her X-1 During the Main High State

In order to determine a meaningful plasma number density range for the disk wind of Her X-1 (in Section 2), we estimate representative outflow properties at different Her X-1 precession phases using previous X-ray spectroscopic observations.

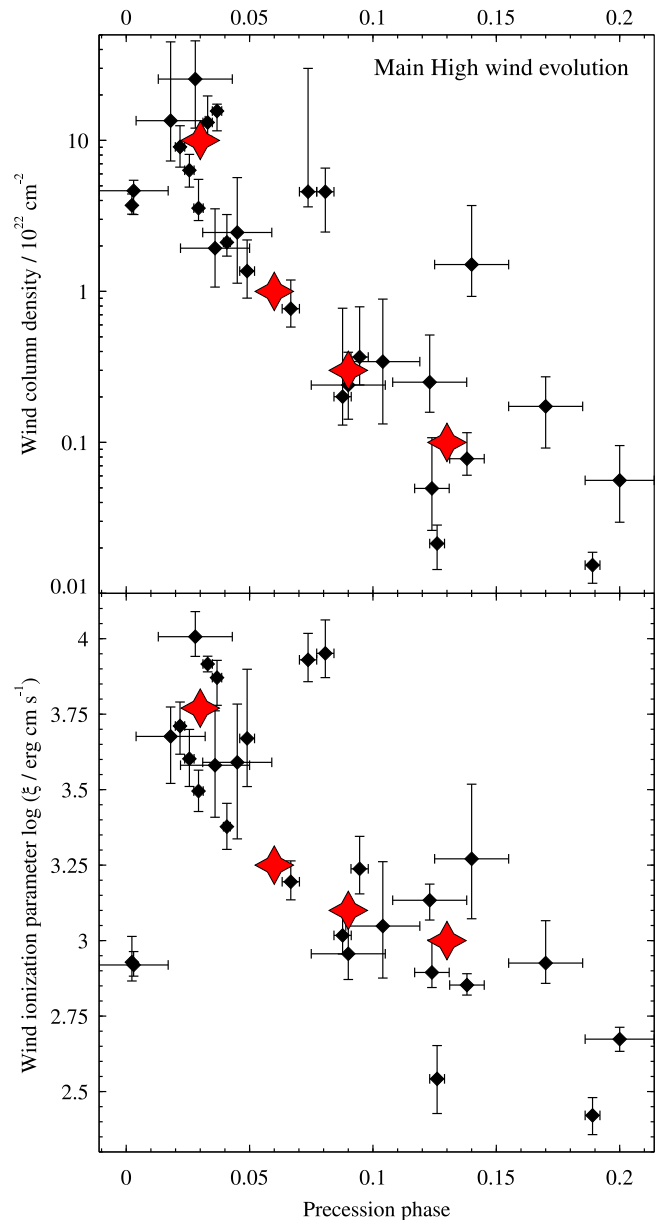


Figure 9. Her X-1 disk wind properties vs. precession phase. The top panel shows the column density, while the lower panel shows the ionization parameter $\log(\xi/\text{erg cm s}^{-1})$. The black points are the wind measurements from Kosec et al. (2023a) using individual XMM-Newton and Chandra observations. The red stars are the estimated representative wind properties used to determine the possible wind density range throughout the main high state of Her X-1.

The measurements at different phases effectively correspond to wind properties sampled at different heights above the disk.

We use the results of Kosec et al. (2023a), where we analyzed 28 XMM-Newton and Chandra observations or observation segments to sample the wind properties throughout the main high state of Her X-1. The wind column density and ionization parameters are shown in black in Figure 9. The representative wind properties are shown in the same figure using red stars. At a precession phase = 0.03, these are determined from the highest-data-quality observation 0865440101, which covers exactly this phase and was analyzed in the methods section of Kosec et al. (2023a). The column density and $\log(\xi/\text{erg cm s}^{-1})$ values for this phase are direct

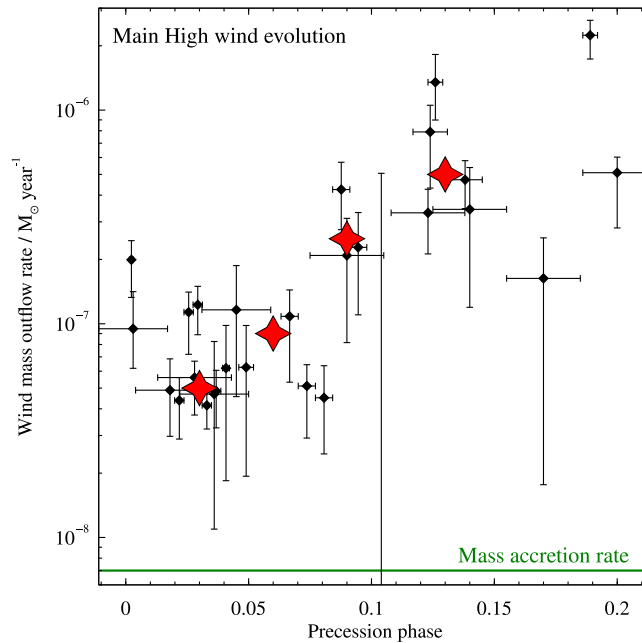


Figure 10. Isotropic (4π) mass outflow rates of Her X-1 vs. disk precession phase. The black points are the mass outflow rate estimates from individual Chandra and XMM-Newton observations (Kosec et al. 2023a). The red stars are the representative mass outflow rates used to obtain the wind number density limits. The green horizontal line is the average measurement of the mass accretion rate through the outer disk of Her X-1 (Boroson et al. 2007), indicating that the solid launch angle of the disk wind must be much smaller than 4π .

Table 3

Representative Accretion Disk Wind Properties of Her X-1 at Different Precession Phases

Precession Phase	Column Density (10^{22} cm^{-2})	Ionization Parameter $\log(\xi/\text{erg cm s}^{-1})$	Isotropic Mass Outflow Rate ($10^{-8} M_{\odot} \text{ yr}^{-1}$)
0.03	10	3.77	5
0.06	1	3.25	9
0.09	0.3	3.10	25
0.13	0.1	3.00	50

spectral fit results. At precession phases of 0.06, 0.09, and 0.13, we estimate the representative wind properties by eye from the individual measurements at comparable precession phases. We note that we ignore the two abnormally high column density and $\log(\xi/\text{erg cm s}^{-1})$ measurements (corresponding to two consecutive observation segments around phase 0.07–0.08), as we consider these data sets to be misfitted (it is unlikely that the wind would change properties so rapidly). These representative wind properties are only used to initially estimate the wind number density limits in Section 2 and as such they do not have to be precise. The wind properties are summarized in Table 3.

We also calculate representative isotropic mass outflow rates at these precession phases using Equation (4). The isotropic outflow rate is calculated by assuming a full volume-filling factor ($C_V = 1$) and a full wind launch solid angle ($\Omega = 4\pi$). In Figure 10, we show the isotropic mass outflow rates for individual Her X-1 main high observations from Kosec et al. (2023a). With the red stars, we show the estimated representative mass outflow rates. Again, the first point (at a precession phase of 0.03) is calculated from the best-fitting wind properties during observation 0865440101. The remaining three points are calculated from the mean wind properties estimated above.

Appendix B EPIC pn Continuum Spectral Variability over the Pulsation Cycle

In Section 4, we split the 1.24 s X-ray pulsation cycle of Her X-1 into 10 phase bins and extracted their EPIC pn spectra. To illustrate the strong X-ray variability over the pulse period, we show the spectra of the odd-numbered phase bins in Figure 11.

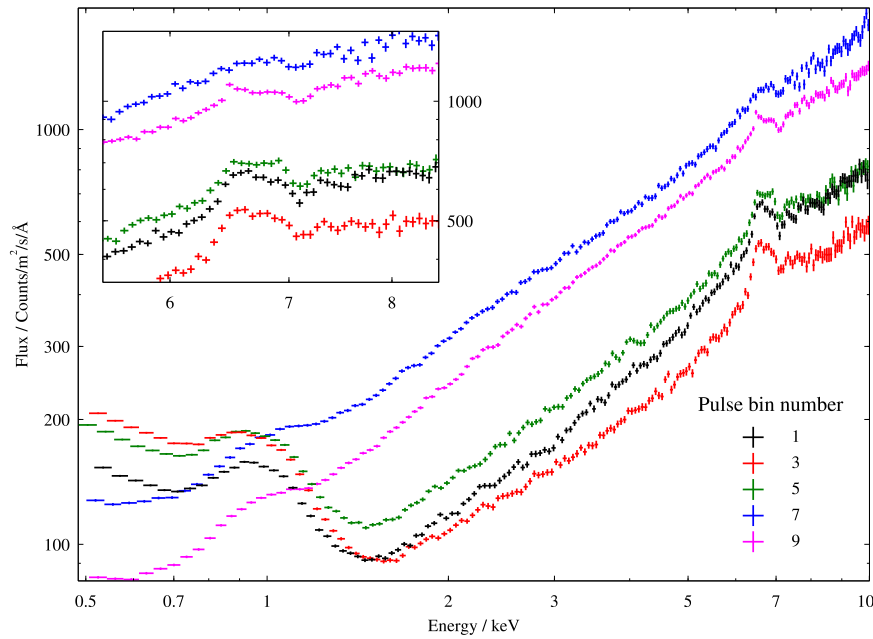


Figure 11. EPIC pn spectra from odd-numbered pulse phase bins. Even-numbered phase bins are omitted for visual clarity. The figure shows the complex spectral variation over the pulse period, where the soft X-rays (<2 keV) peak at a different pulse phase than the hard X-rays (>2 keV). The inset to the top left focuses on the Fe K energy band.

Appendix C

Relative Concentrations of the Ionic States of Fe

To understand the variation of the different ionic column densities of Fe over the X-ray pulsation period and how it relates to the ionization parameter from the PION spectral modeling, we calculate the relative ionic concentrations of the highest-charged Fe states. We apply the ASCDUMP command in SPEX to determine the relative concentrations of Fe XXIV, XXV, XXVI, and XXVII for a range of $\log(\xi/\text{erg cm s}^{-1})$. We use the time-averaged XMM-Newton observation 0865440101 (high-flux period only) as the input SED for these calculations. The results are shown in Figure 12. The gray shaded region indicates the range of best-fitting $\log(\xi/\text{erg cm s}^{-1})$ from the PION pulse-resolved analysis of observation 0865440101. The individual

pulse phase bins have slightly different SEDs, and so their relative concentrations of Fe ions will slightly differ from the values in Figure 12. Nevertheless, the figure gives us helpful insights into how the different Fe ions change in concentration with respect to each other as the X-ray flux varies over the pulsation period of Her X-1.

ORCID iDs

- P. Kosec <https://orcid.org/0000-0003-4511-8427>
 E. Kara <https://orcid.org/0000-0003-0172-0854>
 C. R. Canizares <https://orcid.org/0000-0002-5769-8441>
 A. C. Fabian <https://orcid.org/0000-0002-9378-4072>
 C. Pinto <https://orcid.org/0000-0003-2532-7379>
 I. Psaradaki <https://orcid.org/0000-0002-1049-3182>
 R. Staubert <https://orcid.org/0000-0003-1498-1543>
 D. J. Walton <https://orcid.org/0000-0001-5819-3552>

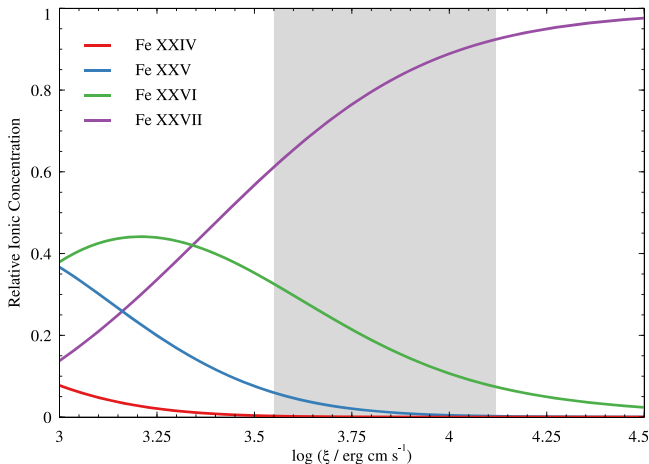


Figure 12. Relative concentrations of the four highest-charged Fe ions—Fe XXIV, XXV, XXVI, and XXVII—vs. the ionization parameter $\log(\xi/\text{erg cm s}^{-1})$. The shaded area indicates the range of the best-fitting ionization parameters from the PION pulse-resolved analysis of XMM-Newton observation 0865440101.

References

- Avakyan, A. L., Lipunova, G. V., & Malanchev, K. L. 2024, *MNRAS*, 527, 3709
 Bachetti, M., Harrison, F. A., Walton, D. J., et al. 2014, *Natur*, 514, 202
 Basko, M. M., & Sunyaev, R. A. 1975, *A&A*, 42, 311
 Begelman, M. C., McKee, C. F., & Shields, G. A. 1983, *ApJ*, 271, 70
 Blandford, R. D., & Payne, D. G. 1982, *MNRAS*, 199, 883
 Boroson, B. S., Vrtilik, S. D., Raymond, J. C., & Still, M. 2007, *ApJ*, 667, 1087
 Brumback, M. C., Hickox, R. C., Fürst, F. S., et al. 2021, *ApJ*, 909, 186
 Canizares, C. R., Davis, J. E., Dewey, D., et al. 2005, *PASP*, 117, 1144
 Carpano, S., Haberl, F., Maitra, C., & Vasilopoulos, G. 2018, *MNRAS*, 476, L45
 Cash, W. 1979, *ApJ*, 228, 939
 Castro Segura, N., Knigge, C., Long, K. S., et al. 2022, *Natur*, 603, 52
 Davidson, K., & Ostriker, J. P. 1973, *ApJ*, 179, 585
 de Plaa, J., Kaastra, J. S., Tamura, T., et al. 2004, *A&A*, 423, 49
 den Herder, J. W., Brinkman, A. C., Kahn, S. M., et al. 2001, *A&A*, 365, L7
 Di Salvo, T., & Sanna, A. 2022, *ASSL*, 465, 87
 Duro, R., Dauser, T., Grinberg, V., et al. 2016, *A&A*, 589, A14
 Ferrigno, C., D’Ai, A., & Ambrosi, E. 2023, *A&A*, 677, A103
 Finger, M. H., Beklen, E., Narayana Bhat, P., et al. 2009, arXiv:0912.3847

- Fürst, F., Grefenstette, B. W., Staubert, R., et al. 2013, *ApJ*, 779, 69
- Gallegos-García, M., Jacquemin-Ide, J., & Kalogera, V. 2023, arXiv:2308.13146
- García, J., Elhoussieny, E. E., Bautista, M. A., & Kallman, T. R. 2013, *ApJ*, 775, 8
- Gerend, D., & Boynton, P. E. 1976, *ApJ*, 209, 562
- Ghosh, P., & Lamb, F. K. 1979, *ApJ*, 232, 259
- Giacconi, R., Murray, S., Gursky, H., et al. 1972, *ApJ*, 178, 281
- Greenstein, J. L., & Oke, J. B. 1982, *ApJ*, 258, 209
- Gu, L., Kaastra, J., Rogantini, D., et al. 2023, *A&A*, 679, A43
- Hickox, R. C., Narayan, R., & Kallman, T. R. 2004, *ApJ*, 614, 881
- Huppenkothen, D., Bachetti, M., Stevens, A., et al. 2019a, *JOSS*, 4, 1393
- Huppenkothen, D., Bachetti, M., Stevens, A. L., et al. 2019b, *ApJ*, 881, 39
- Jansen, F., Lumb, D., Altieri, B., et al. 2001, *A&A*, 365, L1
- Jimenez-Garate, M. A., Raymond, J. C., Liedahl, D. A., & Hailey, C. J. 2005, *ApJ*, 625, 931
- Kaastra, J. S., Mewe, R., & Nieuwenhuijzen, H. 1996, in *UV and X-ray Spectroscopy of Astrophysical and Laboratory Plasmas* (Tokyo: Universal Academy Press), 411
- Kaastra, J. S., Steenbrugge, K. C., Raassen, A. J. J., et al. 2002, *A&A*, 386, 427
- Katz, J. I. 1973, *NPhS*, 246, 87
- Kosec, P., Fabian, A. C., Pinto, C., et al. 2020, *MNRAS*, 491, 3730
- Kosec, P., Kara, E., Fabian, A., et al. 2023a, *NatAs*, 7, 715
- Kosec, P., Kara, E., Fabian, A. C., et al. 2022, *ApJ*, 936, 185
- Kosec, P., Kara, E., Fabian, A. C., et al. 2023b, *ApJ*, 959, 51
- Kosec, P., Pasham, D., Kara, E., & Tombesi, F. 2023c, *ApJ*, 954, 170
- Kosec, P., Pinto, C., Walton, D. J., et al. 2018, *MNRAS*, 479, 3978
- Kotani, T., Ebisawa, K., Dotani, T., et al. 2000, *ApJ*, 539, 413
- Kretschmar, P., El Mellah, I., Martínez-Núñez, S., et al. 2021, *A&A*, 652, A95
- Krolik, J. H., & Kriss, G. A. 1995, *ApJ*, 447, 512
- Leahy, D. A., & Abdallah, M. H. 2014, *ApJ*, 793, 79
- Lee, J. C., Reynolds, C. S., Remillard, R., et al. 2002, *ApJ*, 567, 1102
- Li, C., Kaastra, J. S., Gu, L., & Mehdipour, M. 2023, *A&A*, 680, A44
- Luminari, A., Nicastro, F., Krongold, Y., Piro, L., & Thakur, A. L. 2023, *A&A*, 679, A141
- Marino, A., Anitra, A., Mazzola, S. M., et al. 2022, *MNRAS*, 515, 3838
- Marsh, T. R. 2005, *Ap&SS*, 296, 403
- Marsh, T. R., & Horne, K. 1988, *MNRAS*, 235, 269
- Mehdipour, M., Kaastra, J. S., & Kallman, T. 2016, *A&A*, 596, A65
- Mewe, R., & Schrijver, J. 1978, *A&A*, 65, 99
- Miller, J. M., Kaastra, J. S., Miller, M. C., et al. 2015, *Natur*, 526, 542
- Miller, J. M., Raymond, J., Fabian, A., et al. 2006, *Natur*, 441, 953
- Muñoz-Darias, T., Jiménez-Ibarra, F., Panizo-Espinar, G., et al. 2019, *ApJL*, 879, L4
- Muñoz-Darias, T., & Ponti, G. 2022, *A&A*, 664, A104
- Nandra, K., Barret, D., Barcons, X., et al. 2013, arXiv:1306.2307
- Neilsen, J., & Degenaar, N. 2023, arXiv:2304.05412
- Neilsen, J., Remillard, R. A., & Lee, J. C. 2011, *ApJ*, 737, 69
- Nicastro, F., Fiore, F., Perola, G. C., & Elvis, M. 1999, *ApJ*, 512, 184
- Nixon, C. J., & Pringle, J. E. 2020, *A&A*, 636, A34
- Pinto, C., & Kosec, P. 2023, *AN*, 344, e20220134
- Pinto, C., Middleton, M. J., & Fabian, A. C. 2016, *Natur*, 533, 64
- Prinja, R. K., Ringwald, F. A., Wade, R. A., & Knigge, C. 2000, *MNRAS*, 312, 316
- Proga, D., Stone, J. M., & Kallman, T. R. 2000, *ApJ*, 543, 686
- Rogantini, D., Mehdipour, M., Kaastra, J., et al. 2022, *ApJ*, 940, 122
- Sadula, D. R., Bautista, M. A., García, J. A., & Kallman, T. R. 2023, *ApJ*, 946, 93
- Sánchez-Sierras, J., & Muñoz-Darias, T. 2020, *A&A*, 640, L3
- Scott, D. M., Leahy, D. A., & Wilson, R. B. 2000, *ApJ*, 539, 392
- Shakura, N. I., & Sunyaev, R. A. 1973, *A&A*, 500, 33
- Staubert, R., Klochkov, D., & Wilms, J. 2009, *A&A*, 500, 883
- Steenbrugge, K. C., Kaastra, J. S., Crenshaw, D. M., et al. 2005, *A&A*, 434, 569
- Strohmer, T. E., Altamirano, D., Arzoumanian, Z., et al. 2019, *ApJL*, 878, L27
- Strüder, L., Briel, U., Dennerl, K., et al. 2001, *A&A*, 365, L18
- Tananbaum, H., Gursky, H., Kellogg, E. M., et al. 1972, *ApJL*, 174, L143
- Tetarenko, B. E., Lasota, J. P., Heinke, C. O., Dubus, G., & Sivakoff, G. R. 2018, *Natur*, 554, 69
- Titarchuk, L. 1994, *ApJ*, 434, 570
- Tomaru, R., Done, C., & Mao, J. 2023, *MNRAS*, 518, 1789
- Tombesi, F., Cappi, M., Reeves, J. N., et al. 2010, *A&A*, 521, A57
- Truemper, J., Pietsch, W., Reppin, C., et al. 1978, *ApJL*, 219, L105
- Ueda, Y., Inoue, H., Tanaka, Y., et al. 1998, *ApJ*, 492, 782
- Ueda, Y., Murakami, H., Yamaoka, K., Dotani, T., & Ebisawa, K. 2004, *ApJ*, 609, 325
- van den Eijnden, J., Degenaar, N., Schulz, N. S., et al. 2019, *MNRAS*, 487, 4355
- Verbunt, F. 1993, *ARA&A*, 31, 93
- Weymann, R. J., Morris, S. L., Foltz, C. B., & Hewett, P. C. 1991, *ApJ*, 373, 23
- Wijnands, R. 2004, *NuPhS*, 132, 496
- XRISM Science Team 2020, arXiv:2003.04962
- Zane, S., Ramsay, G., Jimenez-Garate, M. A., Willem den Herder, J., & Hailey, C. J. 2004, *MNRAS*, 350, 506
- Ziółkowski, J., & Zdziarski, A. A. 2018, *MNRAS*, 480, 1580